Bachelorarbeit

zur Erlangung des akademischen Grades
Bachelor of Science (B.Sc.)

Geowissenschaften
Institut für Erd- und Umweltwissenschaften
Mathematisch-Naturwissenschaftliche Fakultät
Universität Potsdam

Land-atmosphere interactions during winter at a permafrost site in Northern Siberia with a focus on water vapor isotopic composition

von

Toni Schmidt
Matrikelnummer 770 881
7. Fachsemester

vorgelegt bei

Prof. Dr. Axel Bronstert
Institut für Erd- und Umweltwissenschaften
Mathematisch-Naturwissenschaftliche Fakultät
Universität Potsdam
Karl-Liebknecht-Str. 24-25
14476 Potsdam

und

PD Dr. Julia Boike
Alfred-Wegener-Institut
Helmholtz-Zentrum für Polar und Meeresforschung
Telegrafenberg A43
14473 Potsdam

Potsdam, den 16. November 2017

Abstract

Land and atmosphere processes influence the isotopic composition of water vapor during winter. Depending on climatic conditions, stable isotope fractionation occurs during each phase change. Thus, isotopes are valuable proxies for air temperatures and tracers of atmospheric moisture. Hourly data records from 01 July 2015 to 30 June 2016 of meteorological and soil parameters and of water vapor isotopic composition from Samoylov Island, Lena Delta, Siberia at 72°22' N, 126°29' E, were investigated to observe local environmental processes during winter and correlations between land, atmosphere, and water vapor isotopes. Winter was defined by the presence of snow (23 September 2015 to 15 May 2016). During winter, water is present in gaseous, liquid, and solid state. The latter was identified in frozen ground, as the active layer froze from 21 October 2015 to 05 June 2016, and on water bodies, as Molo Lake on Samoylov Island had an ice cover from 29 September 2015 to 21 June 2016 and the Lena River had an ice cover from 07 October 2015 to 06 June 2016. Liquid water was though available under the ice cover of Molo and the Lena River. The air was with a mean specific humidity of 1.4 g/kg very dry during winter. Also both $\delta^{18}O$ and δD were very low during winter, with means of -41.3‰ for $\delta^{18}O$ and -299.6‰ for δD. But large ranges of $\delta^{18}O$ and δD were especially observed during four periods of long-term peaks with δ values up to -27.4‰ for $\delta^{18}O$ and -201.0‰ for δD on 27 April 2016. This variability is mostly caused by changes of local air temperatures and humidity levels. With 30.4‰, a high mean of deuterium excess during winter provides information about low humidity conditions and strong kinetic fractionation at evaporation and sublimation at the moisture source location. A slope of 7.4 for the δD-$\delta^{18}O$ correlation during winter suggests local moisture sources. These results show the possibility to explain water vapor isotopic composition with local land and atmosphere processes with the existing data. Additionally, the exploration of recent water vapor on Samoylov Island and its isotopic composition provides findings which can be used as a reference for the assessment of large-scale variations of climate and the hydrological cycle in the Arctic.

Kurzzusammenfassung

Land- und Atmosphärenprozesse beeinflussen die Isotopenzusammensetzung von Wasserdampf im Winter. In Abhängigkeit von den klimatischen Bedingungen tritt eine Fraktionierung stabiler Isotope während jedes Phasenwechsels auf. Somit sind Isotope wertvolle Proxies der Lufttemperatur und Luftfeuchtigkeit. Datensätze mit stündlichen Aufzeichnungen vom 01. Juli 2015 bis 30. Juni 2016 von meteorologischen Parametern und Bodenparametern, sowie Wasserdampfisotopenzusammensetzung von der Insel Samoylov, Lena Delta, Sibirien (72°22‘ N, 126°29’ E), wurden untersucht, um lokale Umweltprozesse im Winter und Korrelationen zwischen Land, Atmosphäre und Wasserdampfisotopen zu bestimmen. Winter wurde durch vorhandenen Schnee definiert (23. September 2015 bis 15. Mai 2016). Im Winter ist Wasser in gasförmigem, flüssigem und festem Zustand vorhanden. Letzterer wurde in gefrorenem Boden identifiziert, da der *active layer* vom 21. Oktober 2015 bis zum 05. Juni 2016 einfrierte, und auf Wasserkörpern, da der Molo-See auf der Insel Samoylov vom 29. September 2015 bis zum 21. Juni 2016 und die Lena vom 07. Oktober 2015 bis 06. Juni 2016 eine Eisschicht hatten. Flüssiges Wasser war jedoch unter der Eisschicht von Molo und Lena vorhanden. Die Luft war im Winter mit einer mittleren spezifischen Feuchtigkeit von 1,4 g/kg sehr trocken. Sowohl δ^{18}O als auch δD waren im Winter mit 41,3‰ (δ^{18}O) und 299,6 ‰ (δD) sehr niedrig. Große Wertebereiche von δ^{18}O und δD wurden jedoch besonders während vier Perioden, mit δ-Werten bis zu 27,4‰ (δ^{18}O) und 201,0‰ (δD) am 27. April 2016, beobachtet. Diese Variabilität wird hauptsächlich durch Änderungen der lokalen Lufttemperatur und der Luftfeuchtigkeit verursacht. Mit 30,4‰ im Winter liefert ein hoher *deuterium excess* Informationen über niedrige Luftfeuchtigkeit und starke kinetische Fraktionierung bei Evaporation und Sublimation am Ort der Wasserdampfbildung. Eine Steigung von 7.4 für die δD-δ^{18}O-Korrelation im Winter deutet auf lokale Feuchtigkeitsquellen hin. Diese Ergebnisse zeigen die Möglichkeit, die Wasserdampfisotopenzusammensetzung mit lokalen Land- und Atmosphärenprozessen anhand der vorhandenen Daten zu erklären. Darüber hinaus liefert die Erforschung von rezentem Wasserdampf auf der Insel Samoylov und deren Isotopenzusammensetzung Erkenntnisse, die als Referenz für die Bewertung von großräumigen Variationen des Klimas und des Wasserkreislaufs in der Arktis dienen können.

Contents

List of figures

List of tables

List of abbreviations

AWI	Alfred-Wegener-Institute Helmholtz-Center for Polar and Marine Research
D	deuterium
d	deuterium excess [‰]
Dsn	snow depth [cm]
GMWL	global meteoric water line
Hrel	relative humidity [%]
Hsp	specific humidity [g/kg]
IP1	isotope peak period 1
IP2	isotope peak period 2
IP3	isotope peak period 3
IP4	isotope peak period 4
Iso-Arc	Isotopes in the Arctic atmospheric water cycle
LWi	incoming long-wave radiation [W/m^2]
LWo	outgoing long-wave radiation [W/m^2]
Patm	atmospheric pressure [kPa]
prec	liquid precipitation [mm]
R	isotopic ratio
r	Pearson correlation coefficient
ρsn_{rel}	relative snow density [%]
Rn	net radiation [W/m^2]
SMOW	Standard Mean Ocean Water
SPARC	Sensitivity of Permafrost in the Arctic
sub	sublimation [mm]
SWE	snow water equivalent [cm]
SWi	incoming short-wave radiation [W/m^2]
SWo	outgoing short-wave radiation [W/m^2]
Tair	air temperature [°C]
Ts	soil temperature [°C]
VSMOW	Vienna Standard Mean Ocean Water
vwc	soil liquid volumetric water content [%]
Wdir	wind direction [°]
WOP	winter onset period
wt	water table [cm]
WTP	winter termination period
Wv	wind speed [m/s]

1 Introduction

Polar regions provide a unique place for the exploration of climate change, as they heat up faster than the rest of the world (ACIA, 2004). These observations can among others be obtained by shifts of atmospheric circulation patterns. As heat is transported to the Arctic by the atmosphere and oceans, these shifts can increase warming in the Arctic (ACIA, 2004). The exploration of recent water vapor and its isotopic composition, provides findings which can be used as a reference for the assessment of large-scale variations of the climate and the hydrological cycle (Bastrikov et al., 2004). Depending on climatic conditions, stable isotope fractionation occurs during each phase change (Clark and Fritz, 1997). Thus, isotopes are valuable proxies for air temperatures and tracers of atmospheric moisture and, hence, are used in many studies.

In 2015, the Iso-Arc (Isotopes in the Arctic atmospheric water cycle) project was launched at the Alfred-Wegener-Institute, Helmholtz-Center for Polar and Marine Research (AWI), aiming at documenting the atmospheric hydrological cycle with a focus on North Atlantic and Arctic oceans (Bonne et al., 2016). Among others, an in-situ surface observation on the island of Samoylov Island, Lena Delta, Northern Siberia at 72°22’ N, 126°29’ E, provides high-resolution data of water vapor isotopic composition. Since 1998, the research group SPARC (Sensitivity of Permafrost in the Arctic) of the AWI runs automated measurements on Samoylov Island to provide an extensive data set of meteorological, soil, and waterbody parameters.

The objective of this thesis is to examine land-atmosphere interactions during winter on Samoylov Island and find correlations with water vapor isotopic composition. For this purpose, data of daily records from 01 July 2015 to 30 June 2016 of meteorological, soil, and water vapor isotope parameters have been used for numerical and graphical investigations.

2 Scientific background

2.1 Periglacial environment

Permafrost

In the Northern Hemisphere, approximately 23.9% (Zhang et al., 2008) of the land area is underlain by permafrost: ground defined to be at or below 0 °C for at least two consecutive years (Permafrost Subcommittee, 1988). Above the permafrost table lies a seasonally freezing and thawing layer, called active layer. Depending on various regional distributions, different types of permafrost can be defined (Brown et al., 1997). Two major types according land surface are continuous and discontinuous permafrost (including sporadic and isolated permafrost). Additionally, subsea permafrost exists, which is underneath the ocean floor (Permafrost Subcommittee, 1988). Continuous permafrost exists, if it occurs “everywhere beneath the exposed land surface throughout a geographic region with the exception of widely scattered sites” (Permafrost Subcommittee, 1988), whereas taliks (layers of unfrozen ground) can exist (Permafrost Subcommittee, 1988). Samoylov Island, the study site of this thesis, is part of a region underlain by continuous permafrost in the Siberian Arctic.

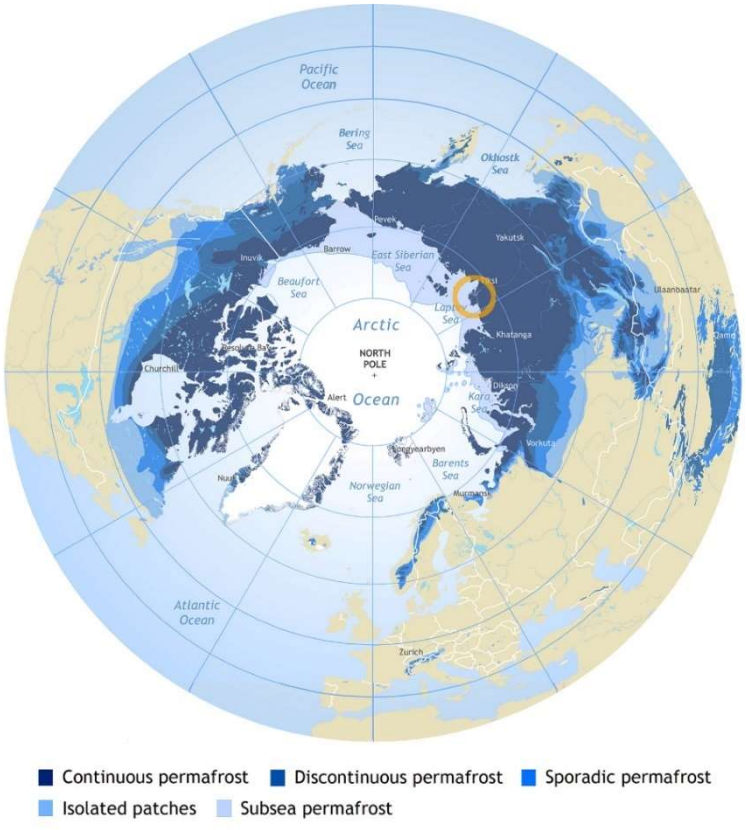

Figure 2.1. Map of the distribution of different types of permafrost on the Northern Hemisphere after Brown et al. (1997), created by the International Permafrost Association. As shown, permafrost is mostly found in circumpolar or high-altitude areas. The orange circle is highlighting the position of the Lena River Delta.

Water vapor in the Arctic

In the Arctic, water exists in all three phases (solid, liquid, vapor) above and below ground (Woo, 2012). Water vapor origins can be remote and transported by convective air mass movements, or local, as it is regionally recycled through evaporation/sublimation and precipitation in the same place (Woo, 2012). Also plant transpiration is a local origin of vapor in tundra regions. But most ground in the Arctic is barren or covered by non-transpiring plants like mosses and lichens (Woo, 2012).

In winter, the ground is covered by snow and sublimation is the most important local water vapor source. After Liston and Sturm (2004), the snow water equivalent (*SWE*) on the ground, precipitation (*prec*), and sublimation (*sub*), are the most important elements of the hydrological cycle in the Arctic during winter and are related by:

$$SWE = prec - sub \tag{1}$$

SWE quantifies the amount of water a snowpack contains and is calculated by:

$$SWE = Dsn \cdot \rho \mathrm{sn}_{\mathrm{rel}} \tag{2}$$

where *Dsn* is the snow depth, and ρsn_{rel} is the relative density of snow, *i.e.* the ratio to the density of water (Dingman, 2015, Woo, 2012).

Sublimation is an essential fraction (10–50%) of total precipitation during winter (Liston and Sturm, 2004). As precipitation, sublimation, and redistribution of snow control the snow cover, they control the land surface and thus the albedo (Liston and Sturm, 2004). Different theories exist concerning the impacts on sublimation. After Schmidt (1972), strong winds are mostly affecting the rates of sublimation, due to the increase of particle surface. But also low humidity levels enhance high sublimation rates (Schmidt, 1972).

2.2 Isotopes

Water vapor isotopic composition

Isotopes are variants of the same chemical element which differ from each other by their masses, determined by the number of neutrons present in the nucleus, while the number of protons are the same. The mass differences of isotopes affect their physical properties.

Both elements of water (hydrogen and oxygen) have different isotopes. Oxygen has three stable isotopes (^{16}O, ^{17}O, ^{18}O), hydrogen has two (^{1}H, ^{2}H), where ^{2}H is commonly named as deuterium and abbreviated with D.

Table 2.1. Stable isotopes of oxygen and hydrogen with their respective number of protons and neutrons. The atomic mass is equal to the number of nucleons (proton and neutrons) and masses are rounded to integers. Its unit is the unified atomic mass unit (u). All values are after Riedel (2010).

Isotope	Number of protons	Number of neutrons	Atomic mass [u]	Natural abundance [%]
^{16}O	8	8	16	99.759
^{17}O	8	9	17	0.035
^{18}O	8	10	18	0.204
^{1}H	1	0	1	99.985
D	1	1	2	0.015

The different isotopes cause numerous varieties of water molecules, named isotopologues, which differ in their mass. In order to explore the water cycle three isotopologues are commonly used: $^{1}H_2{}^{16}O$ is the most prevalent isotopologue (with a mass of 18 u), $^{1}HD^{16}O$ (with a mass of 19 u), and $^{1}H_2{}^{18}O$ (with a mass of 20 u) (Steen-Larsen et al., 2013, Bonne et al., 2014). In addition, their saturation vapor pressure differs (Clark and Fritz, 1997) and anticorrelates with their respective atomic mass. As a consequence, heavier isotopologues have a lower saturation vapor pressure (Clark and Fritz, 1997).

In the following, the term isotopes is used to describe isotopologues.

Fractionation

Differences in atomic mass cause varying reaction rates for isotopes of the same element (Clark and Fritz, 1997). This leads to unequal repartition of isotopes among different reservoirs for the same reactions. This phenomenon is called fractionation and occurs during phase changes (Dansgaard, 1964). Two types of fractionation are distinguished: equilibrium and non-equilibrium (kinetic) fractionation (Clark and Fritz, 1997).

For equilibrium fractionation, alone the different bond strength of isotopes with varying atomic mass cause different reaction rates (Clark and Fritz, 1997). The lower the mass of an isotope of the same element, the higher the reaction rate (*e.g.* ^{16}O reacts more quickly than ^{18}O in the same reaction). For reactions that run in both directions, the bonds of the participating atoms are constantly breaking and rebuilding. As atoms with stronger bonds (heavy isotopes) have lower reaction rates, they will not react for a longer duration, than atoms with lower bonds (light isotopes). Thus, a different ratio between heavy and light isotopes will develop between the initial and the resulting phase (Clark and Fritz, 1997).

Kinetic fractionation occurs under non-equilibrium conditions, which means that reactions are not in thermodynamic equilibrium. The kinetic effect is particularly important during evaporation and arises from the different diffusivities of the water isotopes $H_2{}^{16}O$, $HD^{16}O$, and $H_2{}^{18}O$ in the air (Dansgaard, 1964). This effect is strongly dominated by meteorological conditions under which evaporation takes place, in particular relative humidity and surface temperature and potentially affected by wind speed (Merlivat and Jouzel, 1979).

Delta notation (δ)

The isotopic ratio R of a sample is calculated by dividing the number of heavy isotopes by the number of light isotopes (*e.g.* $H_2{}^{18}O/H_2{}^{16}O$-ratio or $HD^{16}O/H_2{}^{16}O$-ratio).

With the δ notation, the measured isotopic composition is then commonly expressed in permil (‰). It is calculated by dividing measured ratios of the sample and standard using the following formula (Clark and Fritz, 1997):

$$\delta_{\text{sample}} = \left(\frac{R_{\text{sample}}}{R_{\text{standard}}} - 1\right) \cdot 1000 \tag{3}$$

For $H_2{}^{18}O/H_2{}^{16}O$ and $HD^{16}O/H_2{}^{16}O$ the δ notations are calculated by:

$$\delta^{18}\text{O} = \left(\frac{\left(\frac{{H_2}^{18}O}{{H_2}^{16}O}\right)_{\text{sample}}}{\left(\frac{{H_2}^{18}O}{{H_2}^{16}O}\right)_{\text{VSMOW}}} - 1\right) \cdot 1000 \tag{4}$$

$$\delta\text{D} = \left(\frac{\left(\frac{HD^{16}O}{{H_2}^{16}O}\right)_{\text{sample}}}{\left(\frac{HD^{16}O}{{H_2}^{16}O}\right)_{\text{VSMOW}}} - 1\right) \cdot 1000 \tag{5}$$

VSMOW (Vienna Standard Mean Ocean Water) is the most common standard and corresponds to the mean isotopic value of the average oceanic surface water. By definition, both $\delta^{18}O$ and δD of VSMOW have a value of 0‰. If a sample is enriched in heavy isotopes compared to the ocean water, the δ values are positive. Vice versa, if a sample is depleted in heavy isotopes, the corresponding δ values are negative (Clark and Fritz, 1997).

Global meteoric water line

On a global scale, the relationship between $\delta^{18}O$ and δD of fresh surface waters is predictable (Craig, 1961). The isotopic composition of meteoric waters all over the world were measured by Craig (1961), who found a linear correlation between $\delta^{18}O$ and δD and isotopic depletion relative to the initial ocean water. This linear correlation is called global meteoric water line (GMWL) and described by the following equation:

$$\delta\text{D} = 8 * \delta^{18}\text{O} + 10 \tag{6}$$

If evaporation occurs, a shift from the GMWL is the result and leads to local meteoric water lines (LMWL) with lower slope and intercept than the GMWL. The meaning of the GMWL and the shifts from it is shown in Figure 2.2.

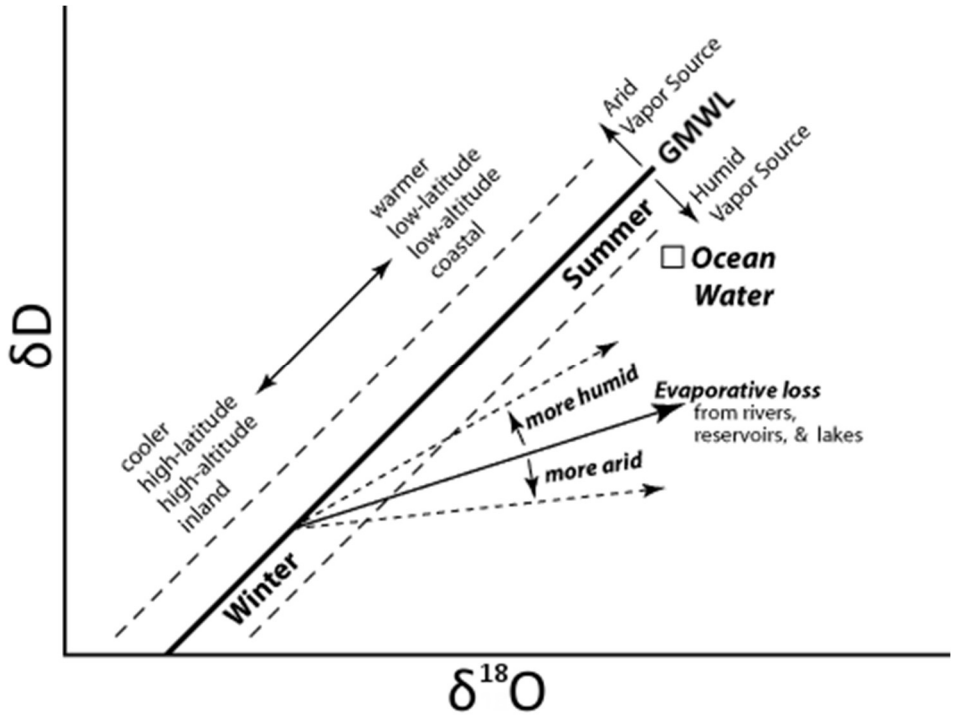

Figure 2.2. δD-δ^{18}O diagram illustrating shifts from the global meteoric water line (GMWL) based on a graphic by SAHRA (2005) with the GMWL as the thick line and areas around it, to which certain climatic and geographic conditions are attributed due to air temperature dependency of equilibrium fractionation during condensation (Craig, 1961). The thin line represents evaporative loss. It has a lower slope due to the humidity dependency of kinetic fractionation during evaporation: the lower the humidity the lower the slope (Dansgaard, 1964).

Deuterium excess (*d*)

Condensation is a process mostly occurring under equilibrium conditions (*i.e.* at 100% relative humidity), whereas kinetic conditions dominate at evaporation due to differences in humidity conditions (Clark and Fritz, 1997). During evaporation, the residual liquid water will be enriched in heavy isotopes, while the developing vapor will be depleted in heavy isotopes (Clark and Fritz, 1997) and will have a relative excess of D compared to ^{18}O, which can also be due to a depletion of ^{18}O. If plotted into a δD-δ^{18}O diagram, this is displayed by the lower slope compared to the GMWL, which strongly depends on relative humidity levels at the moisture source. If this vapor condenses again, its rain water will have a higher δ^{18}O and δD compared to the vapor and in a δD-δ^{18}O diagram it will follow a line parallel to the GMWL due to equilibrium fractionation during condensation. By calculating the difference between both δ values using the coefficient of 8, which is the slope of the GMWL, the effect of equilibrium fractionation

processes is removed and *d* is theoretically only sensitive to kinetic fractionation processes (Dansgaard, 1964).

By definition, the *d* is the deviation to the GMWL (Dansgaard, 1964), as the equation shows:

$$d = \delta\mathrm{D} - 8 \cdot \delta^{18}\mathrm{O} \quad (7)$$

The *d* of ocean surface water is 0‰. But due to kinetic fractionation during evaporation of water at the ocean surface, the global average *d* is 10‰ (Dansgaard, 1964). Local variations of the *d* are mostly affected by relative humidity levels during evaporation (Dansgaard, 1964).

2.3 State of the art

A paper with an aim and region most common to this thesis has been published by Bastrikov et al. (2014). Between April 2012 and April 2013, they recorded the isotopic composition of atmospheric water vapor at the Kourovka astronomical observatory in western Siberia at 57°02' N, 59°33' E, within a forest clearing in the southern Ural Mountains at 300 m above sea level. Isotope measurements were taken at a height of 8 m above ground level. Their data set provides the first records of δD, δ^{18}O, and *d* in this region. Additionally, they installed a meteorological station in July 2012 to assess correlations between isotopic composition and meteorological parameters (*i.e.* air temperature, atmospheric pressure, wind direction, wind speed, relative humidity, and dew point temperature). Relating to the focus of this thesis, their results and observations have been: (1) a seasonal cycle of δD and δ^{18}O with maxima in summer and minima in winter, analogue to the seasonal cycle of air temperature and humidity, (2) a distinct relationship between δD and air temperature and logarithm of humidity, respectively, especially during winter, (4) local humidity variations depend on continental recycling, local evapotranspiration, or convective activity, (5) inaccuracies of isotope measurements occur at low humidity below 0.4 g/kg.

Furthermore, several publications (*e.g.* Kurita, 2011, Steen-Larsen et al., 2013, Bonne et al., 2014, Bonne et al., 2015, and Masson-Delmotte et al., 2015) focus on assessing the isotopic composition of recent atmospheric water vapor in Arctic field sites with different aims.

Kurita (2011) examined the source of water vapor in the Arctic during sea-ice growth to investigate changes in vapor origins in different periods of the year. During summer when the sea-ice extent is decreasing, humidity is increasing and the resulting moisture is distributed in the Arctic. Isotopic composition taken at the research vessel Mirai in 2008 were used as a proxy for the origin of water vapor in the atmosphere. During autumn the *d* of water vapor from the Arctic Ocean was with >20‰ relatively high compared to water vapor deriving from lower latitudes.

In winter, when the sea-ice grows the *d* decreases to around 10‰, which is the global average. In summary, non-local vapor sources dominated during winter, whereas local vapor sources dominated during the rest of the year, when the sea-ice extent is smaller compared to that in winter.

Atmospheric water vapor isotopic composition at the North Greenland Eemian Drilling Project (NEEM) camp, in north-west Greenland at 77°27' N, 51°03' W was recorded and investigated by Steen-Larsen et al. (2013). They collected data at different heights (0.1 m to 13.5 m above snow surface) and found out, that variations in isotopic composition show a distinct relationship to humidity levels and synoptic situations. The variability of isotopic composition is said to be an effect of changing origins of moisture, *i.e.* local or distant. As a result, they identified high *d* values (> 40‰) to be a proxy for vapor originating from distant sources, especially for evaporation at the sea-ice boundary.

Records of isotopic composition of surface water vapor in Ivittuut, South Greenland at 61°12' N, 48°11' W were collected by Bonne et al. (2014). The data set is the first in South Greenland, and also the first one including the winter period in Greenland. Seasonal and synoptic variations of water vapor isotopic composition were assessed concerning moisture sources using a back-trajectory model. Additionally, they found correlations of $\delta^{18}O$ with air temperature (correlation coefficient $r = 0.65$) and logarithm of specific humidity ($r = 0.82$), and of *d* with relative humidity of the moisture source ($r = -0.63$).

An exceptional atmospheric event over Greenland in July 2012 has been examined by Bonne et al. (2015). For nearly a week very warm and moist air advected north-ward, in a process called atmospheric river, and led to significant snow melt. The last occurrence of such an event was in summer 1889. The connection of in-situ measurements of water vapor isotopic composition in Ivittuut, Southwest Greenland and at the NEEM camp, in north-west Greenland with remote sensing data and modeling led to the result, that *d* remained stable over far distance from the western subtropical North Atlantic Ocean to northwest Greenland.

The interplay between water vapor isotopic composition and meteorological signals has been investigated in Ny-Ålesund, Svalbard by Masson-Delmotte et al. (2015). From July to December 2014 they recorded isotope data and found correlations between surface temperature and humidity, and $\delta^{18}O$, and anticorrelations between $\delta^{18}O$ and *d*.

3 Site description

After flowing 4400 km from its source near Lake Baikal through Russia, the Lena River discharges into the Laptev Sea through its vast delta, which is around 280 km wide and extends more than 120 km into the sea (Popov et al., 2016). In the delta, the river disperses into numerous channels and flows around many flat islands of tundra. One of these islands is Samoylov (Figure 3.1). It is located close to the river mouth in the center of the delta and a research station is located on its southern coast at 72°22' N, 126°29' E (Alfred-Wegener-Institute, 2015). The island is characterized by river terraces, ponds, lakes, and an active floodplain (Boike et al., 2013). Since 1998 the island is being visited for the use of many studies and a Russian-German partnership for research in the Siberian tundra has been founded in the same year. Today it is being operated by the Trofimuk Institute for Petroleum Geology and Geophysics, Siberian Branch, Russian Academy of Sciences and gives scientists the chance to study permafrost processes in the Siberian Arctic all over the year.

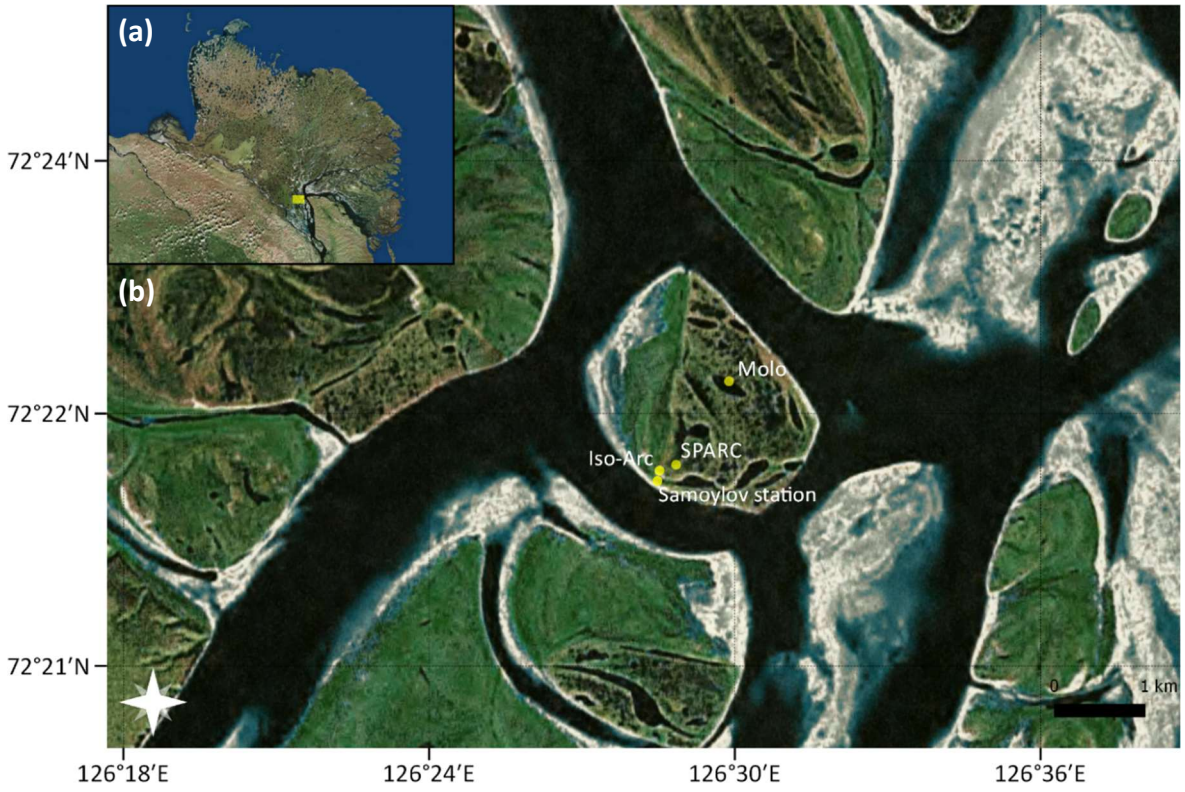

Figure 3.1. Satellite images of the study site. **(a)** shows the Lena River Delta, with a yellow rectangle marking the extent of image (b). The Lena River discharges from SSE into its delta. **(b)** shows Samoylov Island, located in the center of the image. The dot on its southern coast marks the location of the research station, the one NE of it shows the position of the meteorological and soil stations operated by SPARC, and the one N of it that of the water vapor isotope station operated by Iso-Arc, which is around 165 m apart from the SPARC stations. Temperature data of lake Molo is also recorded by SPARC. The satellite images are from the World Imagery base map layer by ESRI.

Long-term observations are among others a key to understanding local environmental processes. The research group SPARC of the AWI runs various automated measurements since 1998 on Samoylov Island to provide an extensive data set of meteorological, soil, and waterbody parameters. Close to the main buildings of the station a field site is used for these investigations.

In 2015, the Iso-Arc (Isotopes in the Arctic atmospheric water cycle) project, funded by AWI's Strategy Fund, was launched, aiming at documenting the atmospheric hydrological cycle with a focus on North Atlantic and Arctic oceans (Bonne et al., 2016). The connection of two running in-situ surface observations on Samoylov Island and the Polarstern research vessel (ocean surface) with partner observations on Svalbard, Iceland, and in Siberia will provide a large-scale network of datasets.

4 Data and methods

Data sets, data processing, and parameters

For this thesis, five data sets were used. Meteorological and soil data were provided as yearly ASCII-files (stations called SaMet2010 and SaSoil2010) containing records of various parameters from 01 January 2015 to 31 December 2016 by the AWI SPARC research group. Isotope data were provided as monthly ASCII-files (called SAM_validated_1h) from 29 June 2015 to 31 August 2016 by the AWI Iso-Arc research group. The temporal resolution of these data sets differs: meteorological and soil records are half-hourly, whereas isotope records are hourly. To work with a consistent data set, a selection of parameters of all three sets has been merged to a single data set with hourly records from 01 July 2015 to 30 June 2016 to examine processes over a period of one full year (366 days, as 2016 has been a leap-year). The finally merged data set consists of 19 parameters, as shown in Table 4.1.

Additionally, temperature data of a lake (called as SaLake2), and photos from a camera station (SaCamE2012) were used. SaLake2 observes lake Molo, which has an area of 39991 m^2, a maximum depth of 5.7 m, and is about 1 km away from the station of Samoylov Island. The temperature data from this station was only used to pick time points of ice-covered and ice-free states without creating publishable plots. The former state can be observed by the timepoint, when all temperature probes, which are in different depths inside of the lake, reach the minimum value after a strong decrease. Whereas the latter state can be observed by the timepoint, when the temperature of surface near water starts to fluctuate. SaCamE2012 runs a camera at the field site, which takes one photo per day.

Data presentation

After creating the final data set, three types of plots were made using RStudio: time-series plots, scatter plots, and wind roses (Guijarro, 2016). For time-series plots, all parameters were plotted above each other as a single diagram. First for the overall year (Figure A.1), later zoomed into periods, which are examined in detail (Figures A.2 to A.7). As the focus is on winter in this thesis, processes in the beginning and at the end of it were picked and highlighted in the time series using colored vertical lines as shown in Figures A.1 to A.3. Every process marked in these figures is named in Tables 5.1 and 5.2. Transparent vertical bars were also added to the time-series plots, representing the periods analyzed in this thesis, as found in Table 4.2.

Table 4.1. List of meteorological, soil, and isotope parameters used for this thesis. Initial data set by SPARC (SaMet2010, SaSoil2010) or Iso-Arc (SAM_validated_1h). Height is above ground surface (no sign) or below it (negative sign). Instrument manufacturer abbreviation K&Z is for Kipp&Zonen, CS is for Campbell Scientific. Values in brackets behind accuracies are environmental conditions or temporal resolution of measurements, with tot/d for daily total.

Initial data set	Parameter	Symbol	Unit	Height	Instrument	Accuracy [±]
SaMet2010	incoming short-wave radiation	*SWi*	W/m²	2.08 m	K&Z CNR4	10% (tot/d)
SaMet2010	outgoing short-wave radiation	*SWo*	W/m²	2.08 m	K&Z CNR4	10% (tot/d)
SaMet2010	incoming long-wave radiation	*LWi*	W/m²	2.08 m	K&Z CNR4	10% (tot/d)
SaMet2010	outgoing long-wave radiation	*LWo*	W/m²	2.08 m	K&Z CNR4	10% (tot/d)
SaMet2010	net radiation	*Rn*	W/m²	2.08 m	K&Z CNR4	10% (tot/d)
SaMet2010	air temperature	*Tair*	°C	2 m	CS HMP45C	0.2 °C (20 °C)
SaMet2010	atmospheric pressure	*Patm*	kPa	0.7 m	CS106	0.03 kPa (20 °C)
SaMet2010	wind direction	*Wdir*	°	3 m	Young 05103	3°
SaMet2010	wind speed	*Wv*	m/s	3 m	Young 05103	0.3 m/s
SaMet2010	relative humidity[A]	*Hrel*	%	2 m	CS HMP45C	2%/3% (</>90%)
SaMet2010	liquid precipitation	*prec*	mm	0 m	CS 52203	2%
SaMet2010	water table[B]	*wt*	cm	-0.115 m	CS TDR100	3 cm
SaMet2010	soil temperature	*Ts*	°C	-0.01 m	CS 109	0.1 °C
SaSoil2010	snow height	*Dsn*	cm	1.08 m	CS SR50A	1 cm
SaSoil2010	soil liquid volumetric water content	*vwc*	%	-0.08 m	CS TDR100	10% (tot/d)
SAM_validated_1h	specific humidity[A]	*Hsp*	g/kg	5 m	Picarro L2140-*i*	0.2 g/kg
SAM_validated_1h	$\delta^{18}O$	$\delta^{18}O$	‰	5 m	Picarro L2140-*i*	0.12‰ (10 s)
SAM_validated_1h	δD	δD	‰	5 m	Picarro L2140-*i*	0.3‰ (10 s)
SAM_validated_1h	deuterium excess	*d*	‰	5 m	Picarro L2140-*i*	1.3‰ (10 s)

[A] Relative humidity (*Hrel*) is the ratio of partial pressure to vapor pressure of water vapor in percent (Dingman, 2015), whereas specific humidity (*Hsp*) is defined as g of water vapor per kg of total air (Dingman, 2015), thus its unit (g/kg) is equal to permil.
[B] The water table (*wt*) is the water level in cm above (positive values) and below (negative values) ground surface. Under frozen conditions, the measuring method does not work anymore. Thus, water table data for soil temperature at 1 cm below ground surface equal or below 0 °C has been removed from the data, due to freezing of the soil.

Scatter plots were only used for investigating the δD-$\delta^{18}O$ relationship. A linear regression line, the global meteoric water line (GMWL), and colorful points for annual and periodic means for $\delta^{18}O$ and δD were added to the plots (Figures 5.1, 5.3, 5.6, 5.9, 5.11, 5.13, and 5.15).

Wind roses (Guijarro, 2016) were created for the overall year and each analyzed period (Figures 5.2, 5.5, 5.8, 5.10, 5.12, 5.14, and 5.16). Northern dominated winds, which range at and around 0° and 360°, are difficult to read in a time-series plot, due to its two dimensions: 0° and 360°

are most remote from each other, albeit they are representing equal wind directions. Maximum long vertical lines in the plot are the result, which can cover different wind directions in between. Nevertheless, this method of representation is used for reasons of consistence in the time-series plots. For an overview of the trends of wind direction and speed for every period, wind roses are valuable, but small-scale information is lost which is important for analyzes of shorter periods as in this thesis.

Data organization

The meteorological, soil, and isotope parameters were categorized into five groups:

- water vapor isotopic composition: $\delta^{18}O$, δD, d
- radiation: *SWi*, *SWo*, *LWi*, *LWo*, *Rn*
- air: *Tair*, *Patm*, *Wdir*, *Wv*, *Hrel*, *Hsp*
- ground surface: *prec*, *wt*, *Dsn*
- soil: *Ts*, *vwc*

In the time series plots, these groups are represented by different colors of the curves.

Table 4.2. Duration of all periods examined in this thesis. These are the winter onset period (WOP), the winter termination period (WTP), and four periods of long-term peaks of isotope δ values (IP1 to IP4, for isotope peak period 1 to 4). Additionally, time periods of winter and deep winter are assigned. All time periods are inclusive of the last day.

Period name	Symbol	Time period
Winter		23 Sep 2015 to 15 Jun 2016
Deep winter		22 Oct 2015 to 14 May 2016
Winter onset period	WOP	21 Sep 2015 to 21 Oct 2015
Winter termination period	WTP	15 May 2016 to 21 Jun 2016
Isotope peak period 1	IP1	07 Nov 2015 to 01 Dec 2015
Isotope peak period 2	IP2	01 Jan 2016 to 12 Jan 2016
Isotope peak period 3	IP3	18 Mar 2016 to 05 Apr 2016
Isotope peak period 4	IP4	23 Apr 2016 to 01 May 2016

In this thesis, winter is defined by the presence of snow. The snow coverage lasted from 23 September 2015 to 15 June 2016, which are 266 days (equal to 72.7% of the total year). The winter onset period (WOP), during which processes occur that initiate winter, is defined as the time between the first record of negative air temperature at 2 m above ground surface on 21 September 2015 and the end of the decrease of soil liquid volumetric water content at 8 cm below

ground surface on 21 October 2015. The winter termination period (WTP), during which processes occur that end winter, is defined as the time between the beginning ablation of snow on 15 May 2016 and the ice-free state of lake Molo on 21 June 2016. Deep winter is defined as the time between the end of the WOP and the beginning of the WTP. Isotope peak periods are defined as single long-term peak events of $\delta^{18}O$ and δD during winter, which stand out due to their great range compared to fluctuations before and after them.

Isotope calibration memory effect

On Samoylov Island, the water vapor isotopic analyzer is calibrated every 25 hours. This procedure includes different vaporized water standards. During very dry climate conditions (specific humidity level below 0.4 g/kg, as defined by Iso-Arc (Bonne, pers. comm.) and recommended in the paper by Bastrikov et al., 2014) falsified variations of $\delta^{18}O$, δD, and d can occur within a few hours after the calibration because of a memory effect. The water standards yield a humidity level much higher than the humidity level of the outside air. Due to this effect, strong variations in the isotope data after calibration gaps are not interpreted as environmental signals. But, as shown in Figure 4.1, none of the δ values during the isotope peak periods (IP1 to IP4), winter onset period (WOP), and winter termination period (WTP) are associated with humidity below this threshold, except for the maximum peak of IP2, whereas the general trend during this period is not influenced by the memory effect.

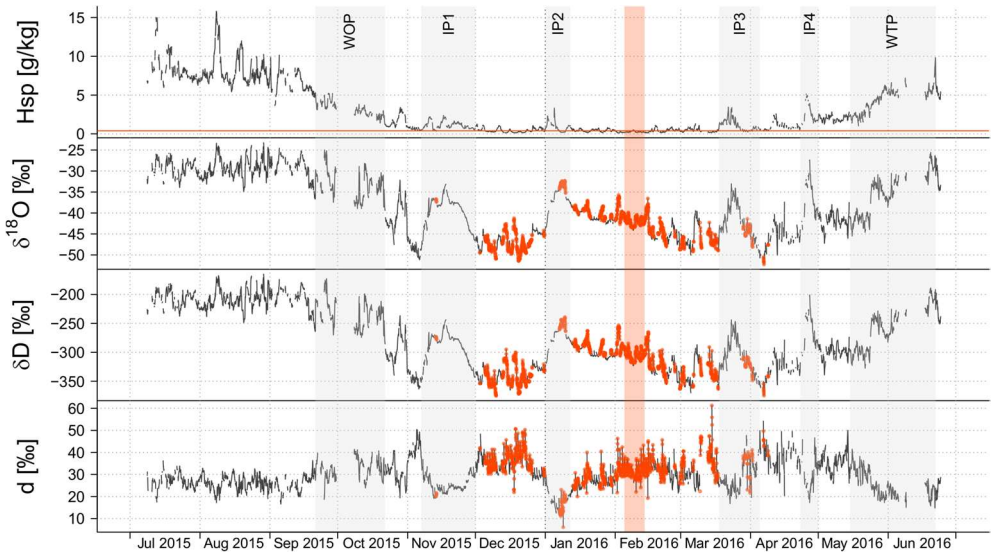

Figure 4.1. Time series plots showing isotope calibration memory effect from 01 July 2015 to 30 June 2016. With specific humidity (*Hsp*), $\delta^{18}O$, δD, and d from top to bottom. Horizontal red line in the *Hsp* plot is the threshold of 0.4 g/kg. In the three plots below, red dots are marking the isotope values recorded at *Hsp* lower than 0.4 g/kg (18.4% of the existing data points). Gray bars signalize the periods that are examined in this thesis. The red bar signalizes a period of very low *Hsp* and is shown in higher temporal resolution in Figure 4.2.

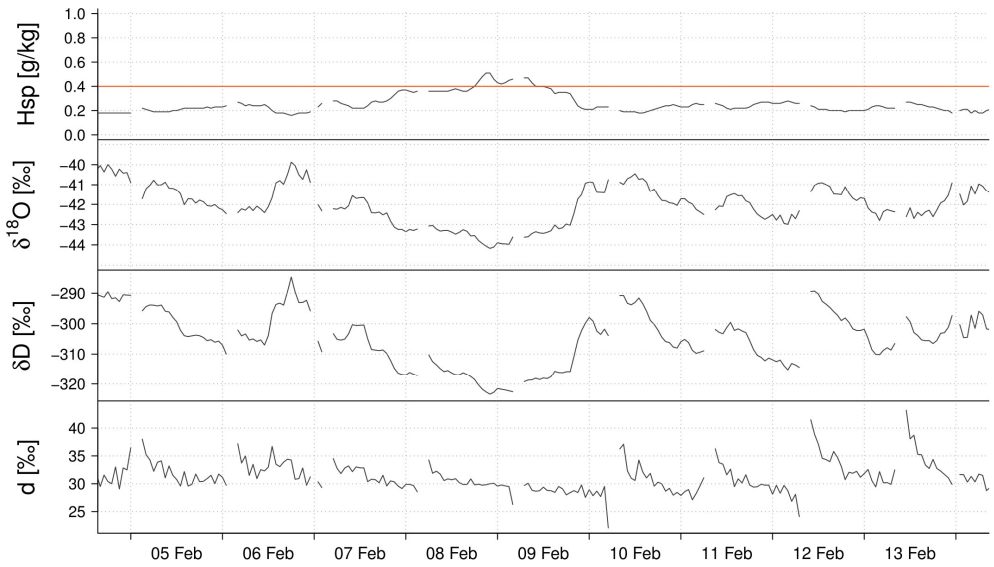

Figure 4.2. Time series plots showing isotope calibration memory effect in detail from 05 to 13 February 2016. With specific humidity (*Hsp*), $\delta^{18}O$, δD, and *d* from top to bottom. Horizontal red line in the *Hsp* plot represents the threshold of 0.4 g/kg. Gaps in the curves are due to calibrations, which occur every 25 hours and have been removed from the data by Iso-Arc.

The curves of *d* in Figure 4.2, show strongly decreasing values directly after the calibration gaps and are possible errors due to contamination with standard water moisture in the water vapor isotopic analyzer. On 09 February, the curve shape does not show the decrease after the calibration gap, as the specific humidity is above 0.4 g/kg during and directly before this timepoint. In addition to these possible *d* errors, curves of δD provide indicators of contamination during calibration, too. Values before and after calibration gaps differ relatively strong for every day, except for 09 February when specific humidity is above the defined threshold. Compared to δD and *d*, the errors are not obviously visible in the curves of $\delta^{18}O$ in this scaling. The periods after calibration of low humidity phases have been prolonged by Iso-Arc to remove the memory effect from the standard.

To keep general trends of water vapor isotopic composition during winter, isotopic δ values and *d* at humidity levels below 0.4 g/kg have not been removed from the data set, but need to be dealt with caution.

5 Results

In this chapter, the data set is being graphically and numerically examined in four sections. First, all data, second, the winter onset period (WOP) and winter termination period (WTP), third, the isotope peak period 1 to 4 (IP1 to IP4), and finally, linear correlations of isotopic composition with meteorological parameters are examined.

Statistical values for all parameters during every period can be found in Table B.1.

5.1 All data

Over the year from 01 July 2015 to 30 June 2016, long-term variabilities and trends of water vapor isotopic composition and of land and atmosphere parameters occurred.

Water vapor isotopic composition

Water vapor isotopic composition show similar trends over the year in Figure A.1, concerning values of $\delta^{18}O$ and δD. From 01 July 2015 until the beginning of the WOP on 21 September 2015, high-frequency variations with ranges of 13.4‰ ($\delta^{18}O$) and 98.4‰ (δD) around mean values of -29.3‰ ($\delta^{18}O$) and -208.2‰ (δD) were recorded. During the WOP, both δ values slightly decrease. In the following deep winter from 22 October 2015 to 15 May 2016, δ values fluctuate around means of -42.6‰ ($\delta^{18}O$) and -309.1‰ (δD) with ranges of 24.9‰ ($\delta^{18}O$) and 174.1‰ (δD), which are larger than before the onset of winter. These large ranges are especially visible during the isotope peak periods 1 to 4 (IP1 to IP4) in Figure A.1. An increasing trend of δ values was recorded during the WTP from 15 May to 21 June 2016, followed by a short time until the end of June 2016 with ranges similar to those before the onset of winter.

d also shows high-frequency variations before the onset of winter around a mean of 26.3‰ with a range of 19.8‰. A slight increase of d is observed during the WOP. In deep winter, mean d increases to 30.7‰. Long-term peaks are opposite to those of $\delta^{18}O$ and δD. During the WTP, d decreases to its minimum of 14.8‰.

Concerning δD-$\delta^{18}O$ correlation, a slope of 7.4 and a δD-intercept of 7.7‰ has been observed, as shown in Figure 5.1.

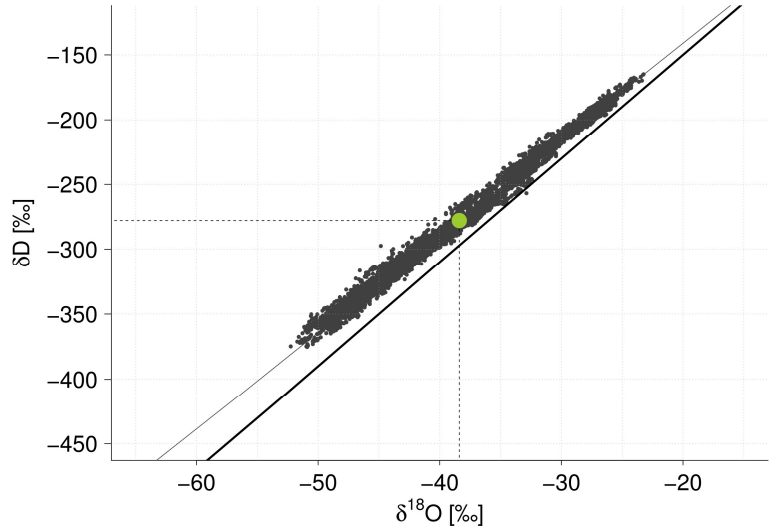

Figure 5.1. δD-δ^{18}O scatter plot for the period from 01 July 2015 to 30 June 2016. The thick line represents the GMWL ($\delta D = 8.0 \cdot \delta^{18}O + 10.0$), the thin line represents the linear regression ($\delta D = 7.4 \cdot \delta^{18}O + 7.7$) with a coefficient of determination of $r^2 = 0.99$. Annual mean of δ^{18}O (-38.4‰) and δD (-277.8‰) is indicated by the green point. The annual mean *d* is 29.3‰.

Radiation

Incoming short-wave radiation has a range of 710.5 W/m^2 around a mean of 86.6 W/m^2 over the year from 01 July 2015 to 30 June 2016. It shows diurnal fluctuations in Figure A.1 but with a decreasing trend of maximum values from July 2015 to November 2015 until it reaches 0 W/m^2 during the day on 20 November 2015 and remains at zero until 26 January 2016, due to polar night. From then on, its daily maxima are constantly increasing until it reaches its maximum in the middle of May 2016. Over the year, outgoing short-wave radiation has a range of 574.8 W/m^2 around a mean of -42.8 W/m^2 and shows diurnal fluctuations in Figure A.1 but with absolute values much lower than those of incoming short-wave radiation. During the WOP from 21 September to 21 October 2015, maximum absolute values before polar night were recorded. From 20 November 2015 to 26 January 2016 outgoing short-wave radiation is constantly zero as well as incoming short-wave radiation. During the WTP from 15 May to 21 June 2016, a rapid increase around the beginning of June 2016 was recorded and the values no longer drop below -104.8 W/m^2.

Both outgoing and incoming long-wave radiation show fluctuations with frequencies mostly lower than that of short-wave radiation and an obvious trend over the year in Figure A.1, with absolute minima in winter (outgoing: -158.58 W/m^2, incoming: 120.1 W/m^2) and absolute maxima in summer (outgoing: -461.4 W/m^2, incoming: 397.4 W/m^2), and means of -270.7 W/m^2 (outgoing) and 241.2 W/m^2 (incoming).

Net radiation has a range of 570.1 W/m^2 and a mean of 14.2 W/m^2. The curve of net radiation shows four periods over the year in Figure A.1. First, diurnal fluctuation with a decreasing trend of maxima is visible from July 2015 to the beginning of the WOP on 21 September 2015. Then a low ranging period of fluctuations with values mostly below 0 W/m^2 but never below -81.5 W/m^2 was recorded from the beginning of the WOP to the middle of March 2016. Then the curve is still showing fluctuations, but with both positive and negative values until 31 May 2016. Finally, daily maxima are rapidly increasing up to 487.6 W/m^2 and diurnal fluctuations up to this intensity follow.

Air

Air temperature at 2 m above ground surface ranges from -41.7 °C to 24.2 °C and has a mean of -11.6 °C. It shows high-frequency fluctuations in Figure A.1 from 01 July 2015 until the end of the WOP on 21 October 2015 followed by mostly low-frequency fluctuations during winter from 23 September 2015 to 15 June 2016, before again high-frequency variations were recorded from the beginning of March 2016. With the beginning of the WOP on 21 September 2015, it drops below the freezing point until if rises above 0 °C during the WTP on 29 May 2016, after a short increase up to 0.7 °C was recorded on 25 and 26 April 2016.

Atmospheric pressure has a mean of 101.4 kPa and a range of 5.8 kPa. It is mostly low (*i.e.* below 101.3 kPa) before and after winter, which lasted from 23 September 2015 to 15 June 2016. Nearly monthly high-pressure periods with values up to 104.3 kPa were recorded during winter, as shown in Figure A.1, though the minimum value of 98.5 kPa is in the beginning of January 2016.

Figure 5.2 shows a wind rose for the overall year from 01 July 2015 to 30 June 2016. According to relative frequency, the dominant wind direction is SSE followed by S. Relatively strong winds (speed above 9 m/s) have another common origin between WSW and NW. Strongest winds are from the end of the WOP on 21 October 2015 until the IP2 in January 2016 with speeds up to 14.5 m/s.

The relative humidity at 2 m above ground surface has a mean of 80.8% and ranges from 44.9% to 99.1%. From 01 July 2015 until the end of the WOP on 21 October 2015, the relative humidity shows high-frequency fluctuations in Figure A.1. During winter from 23 September 2015 to 15 June 2016, low-frequency fluctuations were recorded and a curve mostly parallel to that of air temperature is shown. High relative humidity before and after winter are in contrast to low humidity during winter. Though, its minimum of 44.9% was recorded after winter on 21 June 2016. Specific humidity at 5 m above ground surface ranges from 0.1 g/kg to 15.8 g/kg and is

also relatively low during winter, with a minimum of 0.1 g/kg and a mean of 1.4 g/kg, whereas the overall mean is 2.9 g/kg. Only slight fluctuations of specific humidity occur during winter, as shown in Figure A.1.

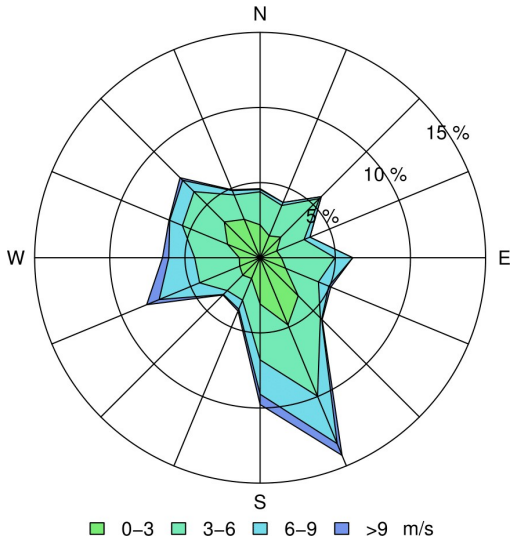

Figure 5.2. Wind rose for the period from 01 July 2015 to 30 June 2016. The circles illustrate relative frequencies from 5% to 20% of wind directions at certain wind speeds at 3 m above ground surface, respectively. A set of four colors is used for different classes of wind speeds in m/s as shown in the legend. The dominant wind direction is SSE.

Ground surface

In total, 133.8 mm of liquid precipitation was recorded and 92.2% of it felt during summer, as visible in Figure A.1. On 26 April 2016 liquid precipitation was recorded with a sum of 4.8 mm and represents the only event during deep winter from 22 October 2015 to 14 May 2016.

The water table has a mean level of 0.4 cm below ground surface and ranges from 3.2 cm below to 3.4 cm above ground surface. It rapidly increases with every liquid precipitation event before it decreases again, respectively. With the onset of negative soil temperature at 1 cm below ground surface on 24 September 2015, its recorded values are no longer usable, as described in chapter 4. First from 05 June 2016, when soil temperature gets positive again, values of the water table are shown in Figure A.1. From 0.7 cm above ground surface it decreases down to 3.2 cm below ground surface during June 2016.

The snow depth has a mean of 15.1 cm and ranges up to 44.9 cm. The first snow fall is not visible in the time series plot in Figure A.1 but on a photo in Figure 5.4, taken by the installed camera. It is first visible on a photo from 21 September and on 23 September 2015 it was measured by the distance sensor. After a short time of accumulation and ablation, another snow fall was recorded by the sensor on 29 September which represents the beginning of a solid snow

cover for the entire winter. At the beginning of the WTP on 15 May 2016 a last and strongest increase of snow height from 35.8 cm to 44.9 cm was recorded. During this period, snow height is decreasing until no snow is left on 15 June 2016.

Soil

Soil temperature at 1 cm below ground surface ranges from -25.9 °C to 19.9 °C and has a mean of -6.9 °C. It shows diurnal fluctuations before the onset of winter on 23 September 2015, as shown in Figure A.1. During the WOP from 21 September to 21 October 2015, it shows a strong zero curtain effect and stays around 0 °C for 28 days with a range of 0.8 °C, before soil liquid volumetric water content at 8 cm below ground surface stops decreasing on 21 October. Afterwards soil temperature shows low-frequency fluctuations and decreases to the minimum of -25.9 °C in February 2016. During the WTP from 15 May to 21 June 2016 it increases again and stays around 0 °C for nearly five days with a range of 1.5 °C, before it reaches positive values on 05 June 2016 and continues with diurnal fluctuations.

Soil liquid volumetric water content at 8 cm below ground surface stays around a mean value of 94.6% from July 2015 to the middle of the WOP on 15 October 2015 before it decreases to a minimum of 8.4% during this period, as shown in Figure A.1. First during the WTP on 08 June 2016 it rapidly increases again to values similar to those before the onset of winter, nine days after it started to increase slightly on 30 May 2016. The overall minimum of soil liquid volumetric water content is 4.6%.

5.2 Winter onset and termination periods

Winter is initiated and ends with environmental processes (Tables 5.1 and 5.2) that are connected with the frozen or liquid state of water. The winter onset period (WOP) lasted 31 days from 21 September to 21 October 2015 and the winter termination period (WTP) lasted 38 days from 15 May to 21 June 2016.

5.2.1 Winter onset period (WOP)

During the winter onset period (WOP), water vapor isotopic δ values show a decreasing trend in Figure A.2. From maxima of -25.0‰ (δ^{18}O) and -172.8‰ (δD) they range down to -39.4‰ (δ^{18}O) and -285.49‰ (δD) around means of -33.4‰ (δ^{18}O) and -235.0‰ (δD). *d* mostly shows opposite trends to δD and δ^{18}O in Figure A.2 with a mean of 32.4‰ and ranges from 18.7‰ to 41.4‰. Concerning δD-δ^{18}O correlation, a slope of 7.1 and a δD-intercept of 2.2‰ has been observed, as shown in Figure 5.3.

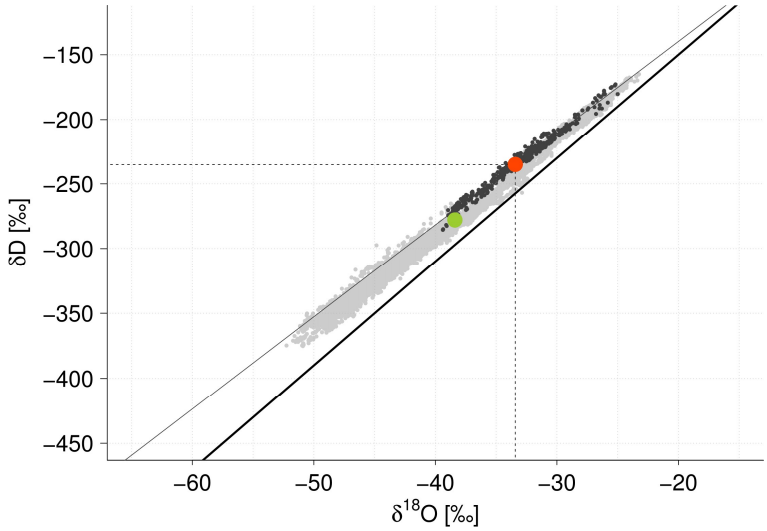

Figure 5.3. δD-δ^{18}O scatter plot for the winter onset period (WOP) from 21 September to 21 October 2015. Gray data points are those of all data from 01 July 2015 to 30 June 2016, black ones are those of the period. The thick line represents the GMWL ($\delta D = 8.0 \cdot \delta^{18}O + 10.0$), the thin line is the linear regression ($\delta D = 7.1 \cdot \delta^{18}O + 2.2$) with a coefficient of determination of $r^2 = 0.98$. Annual mean of δ^{18}O (-38.4‰) and δD (-277.8‰) is indicated by the green point, whereas the red point represents the periodic mean δ^{18}O (-33.4‰) and δD (-235.0‰). Annual mean *d* is 29.3‰, periodic mean is 32.4‰.

On the first day of the WOP on 21 September 2015, air temperature at 2 m above ground surface drops below 0 °C, snow was recorded, and liquid precipitation stops. Air temperature peaks above 0 °C five more times within ten days, whereas the daily average is below the freezing point, as shown in Figure A.2. From 02 October 2015 to 25 April 2016, no air temperature was recorded above 0 °C.

Table 5.1. Environmental processes defining the winter onset period (WOP) as marked in Figures A.1 and A.2 with dashed lines, respectively, which lead to the frozen state of local liquid water. The WOP lasted from 21 September to 21 October 2015, defined by dates of the first and last process.

Date	Period	Parameter	Symbol	Process	Dashed line color
21 Sep 2015	WOP	air temperature	*Tair*	< 0 °C	yellow
23 Sep 2015	WOP	snow depth	*Dsn*	first snow	orange
24 Sep 2015	WOP	soil temperature	*Ts*	0 °C	red
29 Sep 2015	WOP	Molo (lake)	Molo	ice cover	green
07 Oct 2015	WOP	Lena River	Lena	freezing	blue
21 Oct 2015	WOP	soil liquid volumetric water content	*vwc*	constant	magenta

The first snow fall is not visible in the time series but on photos (Figure 5.4), as reported in chapter 5.1. From 23 September, snow reaches heights of 4.2 cm until it completely melts away after three days, when air temperature again rises above 0 °C, as shown in Figure A.2. The second snow accumulation begins on 29 September and is the onset of a continuous snow cover

until the end of winter on 15 June 2016. Within two days it reaches a depth of around 10 cm. By the end of the WOP on 21 October snow is 15.5 cm deep.

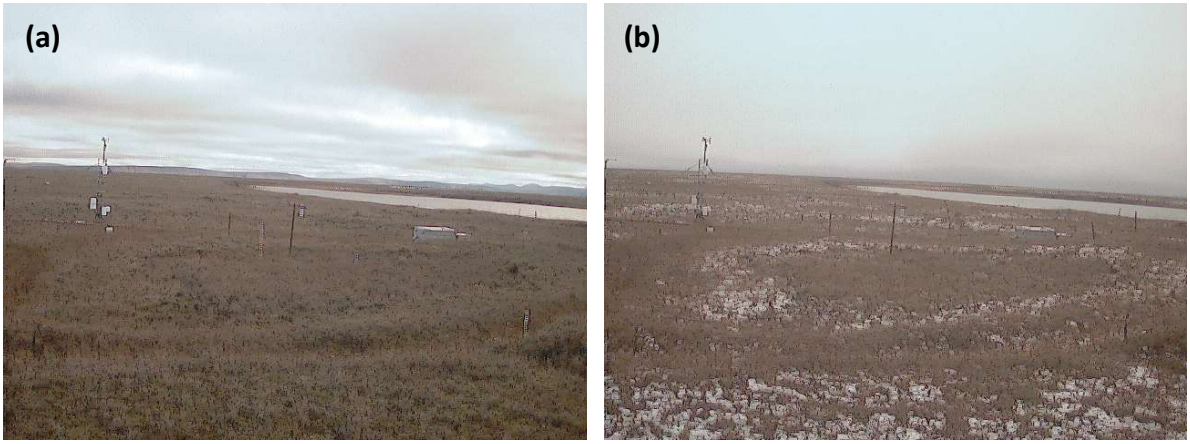

Figure 5.4. Field site pictures around the beginning of the winter onset period (WOP). Both were taken by the camera, **(a)** on 20 September 2015, and **(b)** on 21 September 2015. The first snow on 21 September is not covering the entire ground and hence not recorded by the snow sensor.

On 23 September, soil temperature at 1 cm below ground surface reaches freezing point two days after air temperature and remains around 0 °C for 28 days with a range of 0.8 °C, before soil liquid volumetric water content at 8 cm below ground surface stops decreasing, as shown in Figure A.2.

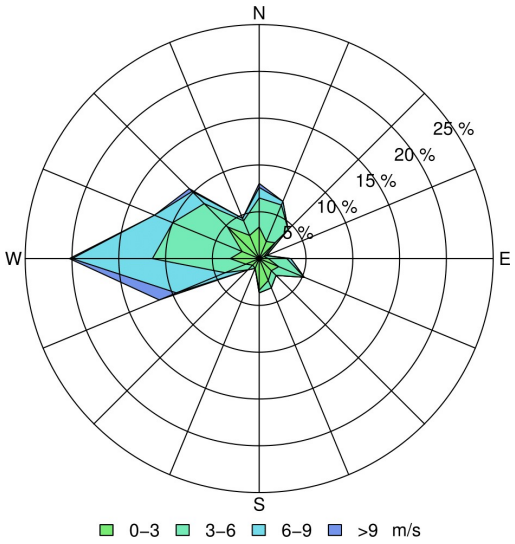

Figure 5.5. Wind rose for the winter onset period (WOP) from 21 September to 21 October 2015. The circles illustrate relative frequencies from 5% to 25% of wind directions at certain wind speeds at 3 m above ground surface, respectively. A set of four colors is used for different classes of wind speeds in m/s as shown in the legend. The dominant wind direction is W.

Most of the residual parameters show a decreasing trend during the WOP: absolute values of short- and long-wave radiation decrease, net radiation decrease too and reaches all-day negative values on 03 October, specific humidity at 5 m above ground surface decrease from a maximum of 5.3 g/kg to a minimum of 1.2 g/kg, whereas the mean relative humidity at 2 m above ground surface remains mostly steady, and the water table is constantly decreasing down to a depth of 1.3 cm below ground surface before soil temperature at 1 cm below ground surface drops below 0 °C and thus leads to the end of reliable water table records, as explained in chapter 4. The observed lake (Molo, see Figure 3.1) has an ice cover from the 29 September and the Lena River starts freezing on 07 October (Bonne et al., 2016).

5.2.2 Winter termination period (WTP)

Delta values of water vapor stable isotopes increase during the WTP. From minimum values of -45.5‰ (δ^{18}O) and -327.5‰ (δD) they reach up to maximum values of -25.6‰ (δ^{18}O) and -188.7‰ (δD) around means of -35.8‰ (δ^{18}O) and -261.2‰ (δD), as shown in Figure A.3. *d* shows opposite trends to δ^{18}O and δD in Figure A.3 and has a mean of 25.3‰ and ranges from 14.8‰ to 41.5‰. Concerning δD-δ^{18}O correlation, a slope of 7.1 and a δD-intercept of -8.3‰ has been observed, as shown in Figure 5.6.

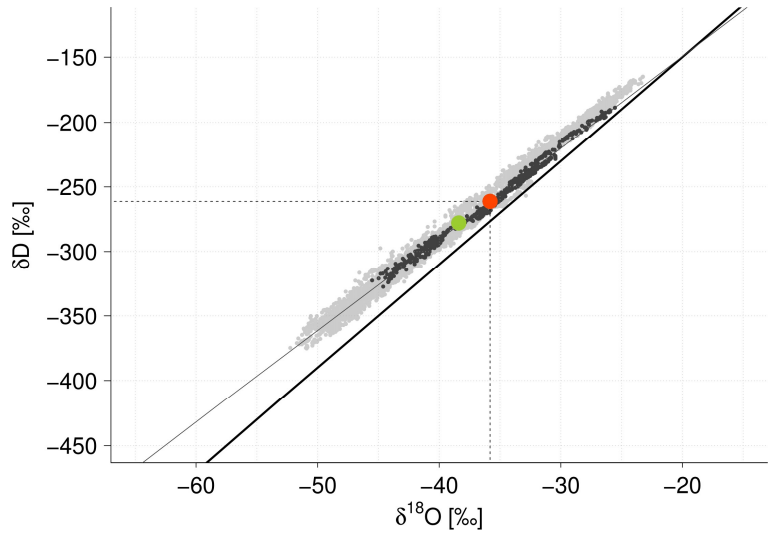

Figure 5.6. δD-δ^{18}O scatter plot for the winter termination period (WTP) from 15 May to 21 June 2015. Gray data points are those of all data from 01 July 2015 to 30 June 2016, black ones are those of the WTP. The thick line represents the GMWL ($\delta D = 8.0 \cdot \delta^{18}O + 10.0$), the thin line represents the linear regression ($\delta D = 7.1 \cdot \delta^{18}O - 8.3$) with a coefficient of determination of $r^2 = 0.99$. Annual mean of δ^{18}O (-38.4‰) and δD (-277.8‰) is indicated by the green point, whereas the red point represents the periodic mean of δ^{18}O (-33.4‰) and δD (-261.2‰). Annual mean *d* is 29.3‰, periodic is 25.3‰.

The WTP is initiated with the onset of snow melt on 15 May after the maximum snow height during the entire winter of 44.9 cm is reached on the same day, as shown in Figure A.3. For 14 days, snow height decreases by an average of 0.5 cm per day, followed by a four-day phase with an average decrease of 6.8 cm per day, before a subsequent melting period for 13 days follows with an average decrease of 0.8 cm per day until no snow is left on 15 June.

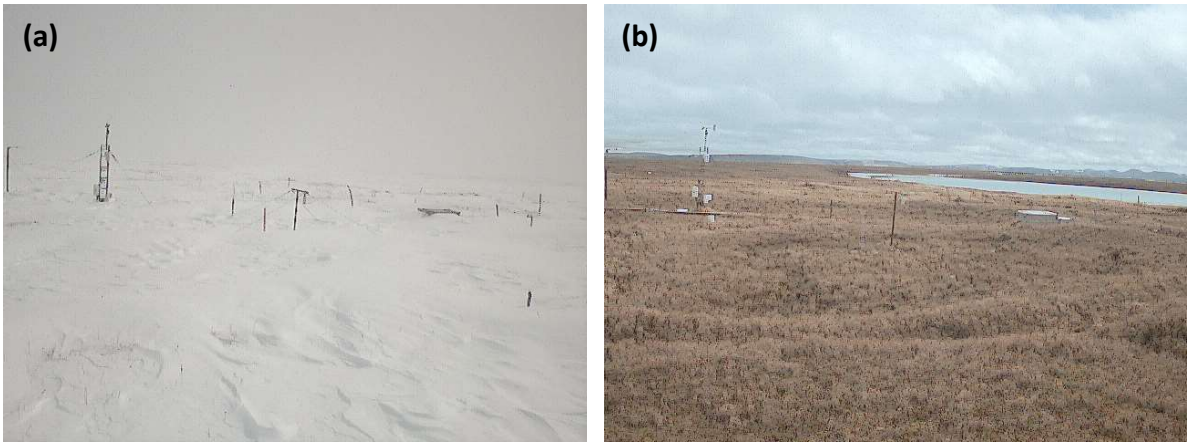

Figure 5.7. Field site pictures during the winter termination period (WTP). Both were taken by the camera, **(a)** on 15 May 2016, and **(b)** on 15 June 2016. The maximum snow height (44.9 cm) of the entire year from 01 July 2015 to 30 June 2016 was on 15 May 2016.

Air temperature at 2 m above ground surface rises above 0 °C on 29 May for the first time after 02 October, except for a short increase up to 0.7 °C on 25 and 26 April. With the positive air temperature, soil temperature at 1 cm below ground surface rapidly increases from -10.1 °C to -1.9 °C within 56 hours, as shown in Figure A.3. On 05 June, it rises above 0 °C, after staying around 0 °C for nearly five days with a range of 1.5 °C. Soil liquid volumetric water content at depths of 8 cm below ground surface rapidly increases from 08 June and within two days it reaches its maximum of 99.4%, nine days after it started to increase slightly on 30 May.

Table 5.2. Environmental processes defining the winter termination period (WTP) as marked in Figures A.1 and A.3 with dashed lines, respectively. The WTP lasted from 15 May to 21 June 2016, defined by dates of the first and last process.

Date	Period	Parameter	Symbol	Process	Dashed line color
15 May 2016	WTP	snow depth	*Dsn*	decreasing	orange
29 May 2016	WTP	air temperature	*Tair*	> 0 °C	yellow
30 May 2016	WTP	soil liquid volumetric water content	*vwc*	increasing	magenta
05 Jun 2016	WTP	soil temperature	*Ts*	> 0 °C	red
06 Jun 2016	WTP	Lena River	Lena	breakup	blue
15 Jun 2016	WTP	snow depth	*Dsn*	no snow	orange
21 Jun 2016	WTP	Molo (lake)	Molo	ice free	green

Additionally, the first air temperature above 0 °C initiates the phase of snow ablation with the highest rate on 29 May, as shown in Figure A.3. This high-rate snow ablation phase is a time of changes for many parameters. Both incoming and outgoing short-wave radiation show diurnal fluctuations before this phase. But daily absolute maxima of the outgoing component rapidly increase during it with values no longer dropping below -104.8 W/m^2 until the end of the WTP on 21 June 2016. Outgoing long-wave radiation shows lower daily maxima than before, as shown in Figure A.3. And daily maxima of net radiation strongly increase as snow ablation accelerates.

The specific humidity at 5 m above ground surface increases from 1.0 g/kg up to 9.8 g/kg during the WTP, while the relative humidity at 2 m above ground surface fluctuates around a mean of 84.7% in Figure A.3.

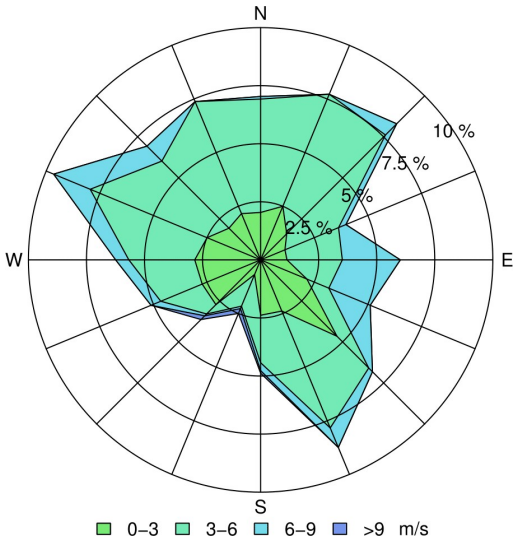

Figure 5.8. Wind rose for the winter termination period (WTP) from 15 May to 21 June 2016. The circles illustrate relative frequencies from 2.5% to 10% of wind directions at certain wind speeds at 3 m above ground surface, respectively. A set of four colors is used for different classes of wind speeds in m/s as shown in the legend. Dominating wind directions are WNW to NE and SSE.

The ice cover of the observed lake (Molo, see Figure 3.1) starts to break up on 01 June until the lake is completely ice free on 21 June. On 06 June, the ice cover of the Lena breaks up (Bonne et al., 2016), which is visible in satellite images from TerraSAR-X, Sentinel-1, and Sentinel-2 (Gorelick et al., 2017)

5.3 Isotope peak periods

5.3.1 Isotope peak period 1 (IP1)

The isotope peak period 1 (IP1) went from 07 November 2015 to 01 December 2015. With a duration of 25 days it is the longest isotope peak period examined in this thesis.

Water vapor isotopic composition

During the IP1, mean δ values are -39.8‰ (δ^{18}O) and -292.5‰ (δD). Twelve days after the end of the WOP on 21 October, both δ^{18}O and δD increase until they peak on 17 November with maxima of -33.1‰ (δ^{18}O) and -243.8‰ (δD), as shown in Figure A.4. *d* has a mean of 25.9‰ and shows an opposite trend to δ^{18}O and δD, but with no such obvious peaks. From a maximum of 38.1‰ it decreases to a minimum of 19.1‰. Concerning δD-δ^{18}O correlation, a slope of 7.0 and a δD-intercept of -12.0‰ has been observed, as shown in Figure 5.9.

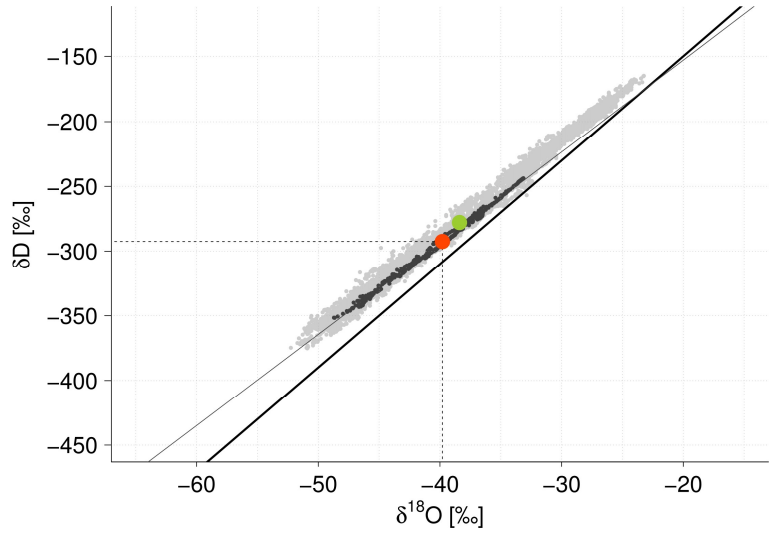

Figure 5.9. δD-δ^{18}O scatter plot for the isotope peak period 1 (IP1) from 07 November to 01 December 2015. Gray data points are those of all data from 01 July 2015 to 30 June 2016, black ones are those of the period. The thick line represents the GMWL ($\delta D = 8.0 \cdot \delta^{18}O + 10.0$), the thin line represents the linear regression ($\delta D = 7.0 \cdot \delta^{18}O - 12.0$) with a coefficient of determination of $r^2 = 1.00$. Annual mean of δ^{18}O (-38.4‰) and δD (-277.8‰) is indicated by the green point, whereas the red point represents the periodic mean of δ^{18}O (-39.8‰) and δD (-292.5‰). Annual mean *d* is 29.3‰, periodic mean is 25.9‰.

Radiation

In Figure A.4, short-wave radiation decreases according to absolute daily maxima, until 0 W/m^2 are constantly reached on 20 November. Outgoing and incoming long-wave radiation peak from the middle of 15 November to the end of 17 November, when the maxima of δ^{18}O and δD are reached. This peak is also visible in the net radiation curve, as it increases up to 0 W/m^2 during these days.

Air

Air temperature at 2 m above ground surface reaches a maximum of -9.3 °C, as isotopic δ values peak and shows an increasing trend before in Figure A.4. Atmospheric pressure has a mean value of 102.2 kPa, which is high-pressure. As δ^{18}O and δD peak, the maximum pressure is reached. Wind direction is showing no obvious variations in Figure A.4 but two dominant directions: WSW and S, as visible in the wind rose in Figure 5.10. A time of high wind speed was recorded on 10 November with a speed up to 13.9 m/s from W.

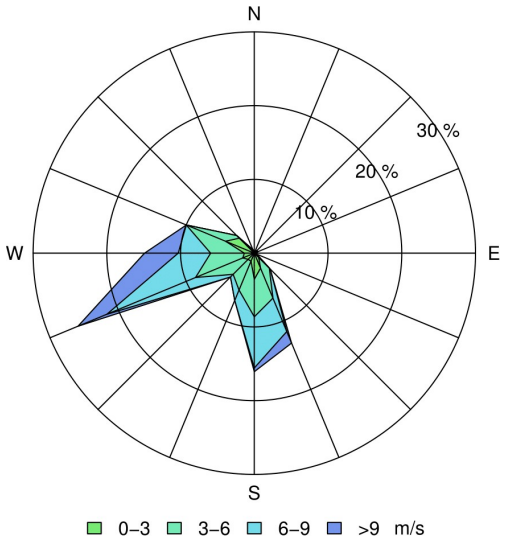

Figure 5.10. Wind rose for the isotope peak period 1 (IP1) from 07 November to 01 December 2015. The circles illustrate relative frequencies from 10% to 30% of wind directions at certain wind speeds at 3 m above ground surface, respectively. A set of four colors is used for different classes of wind speeds in m/s as shown in the legend. Dominant wind directions are WSW and S.

Both relative and specific humidity have their maxima, as δ^{18}O and δD peak, as shown in Figure A.4. Relative humidity at 2 m above ground surface reaches values up to 91.6% and specific humidity at 5 m above ground surface up to 2.4 g/kg.

Ground surface

Snow depth has one characteristic peak from 14 to 18 November in Figure A.4. From a height of around 16 cm it rapidly increases to a maximum of 21.9 cm on 14 November, before it decreases to around 16 cm on 18 November. No events of liquid precipitation were recorded.

Soil

Soil temperature at 1 cm below ground surface also shows a peak in Figure A.4 around the same time as δ^{18}O and δD peak but with longer durations and slopes not as steep. On 18 November,

it reaches its maximum of -1.4 °C. Soil liquid volumetric water content at 8 cm below ground surface only shows slight variations with a range of 2.3% around its mean of 7.8%.

5.3.2 Isotope peak period 2 (IP2)

From 01 January 2016 to 12 January 2016, the isotope peak period 2 (IP2) occurred and thus lasted twelve days.

Water vapor isotopic composition

During the IP2, mean δ values are -36.3‰ (δ^{18}O) and -272.3‰ (δD). A nine-day long increase of δ^{18}O and δD is the major trend, as shown in Figure A.5. On 09 January, both δ values peak to maxima of -32.3‰ (δ^{18}O) and -239.2‰ (δD). These peaks are followed by a decrease until the end of the IP2 on 12 January, with minima of -43.8‰ (δ^{18}O) and -324.8‰ (δD). *d* has a mean of 18.3‰, which is the lowest mean *d* compared to every other examined period. *d* ranges from 6.1‰ to 29.9‰ and shows an opposite trend compared to δ values in Figure A.5 and decreases to 09 January. Concerning δD-δ^{18}O correlation, a slope of 6.9 and a δD-intercept of -22.5‰ has been observed, as shown in Figure 5.11.

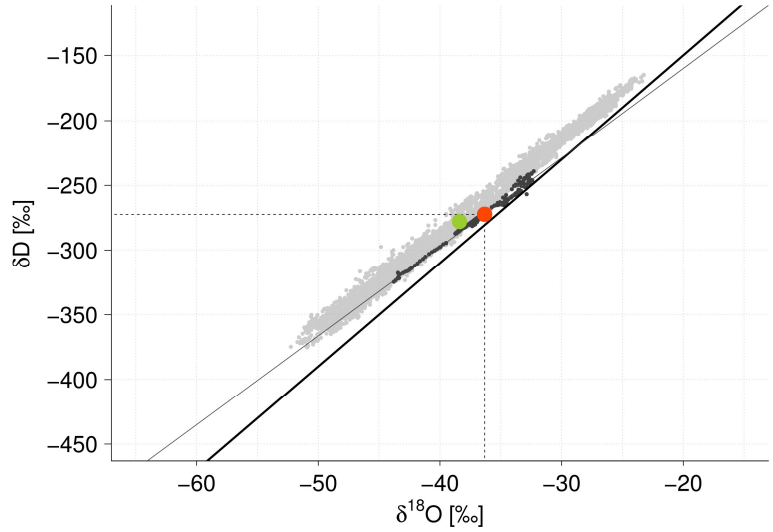

Figure 5.11. δD-δ^{18}O scatter plot for the isotope peak period 2 (IP2) from 01 to 12 January 2016. Gray data points are those of all data from 01 July 2015 to 30 June 2016, black ones are those of the period. The thick line represents the GMWL ($\delta D = 8.0 \cdot \delta^{18}O + 10.0$), the thin line is the linear regression ($\delta D = 6.9 \cdot \delta^{18}O - 22.5$) with a coefficient of determination of $r^2 = 0.99$. Annual mean of δ^{18}O (-38.4‰) and δD (-277.8‰) is indicated by the green point, whereas the red point represents the periodic mean of δ^{18}O (-36.3‰) and δD (-272.3‰). Annual mean *d* is 29.3‰, periodic mean is 18.3‰.

Radiation

Short-wave radiation is zero due to polar night. Outgoing long-wave radiation reaches its absolute minimum on 09 January after a decrease of five days, as shown in Figure A.5. Incoming

long-wave radiation decreases to its minimum between 07 and 09 January. The variations of net radiation are very similar to that of incoming long-wave radiation.

Air

Between 05 and 09 January, air temperature at 2 m above ground surface decreases down to -36.2 °C, followed by an abrupt increase, as shown in Figure A.5. Maximum air temperature is on 04 and 05 January with a peak up to -5.7 °C. As air temperature decreases, atmospheric pressure increases and reaches high-pressure on 06 January until the end of the IP2 on 12 January, after only low-pressure was recorded before. The curve shape of wind speed at 3 m above ground surface in Figure A.5 is very similar to that of air temperature. Between 04 and 05 January it peaks above 14 m/s with directions from W and NW. On 07 January, a strong shift of wind direction was recorded from WNW to SSE. These directions last up to 10 January.

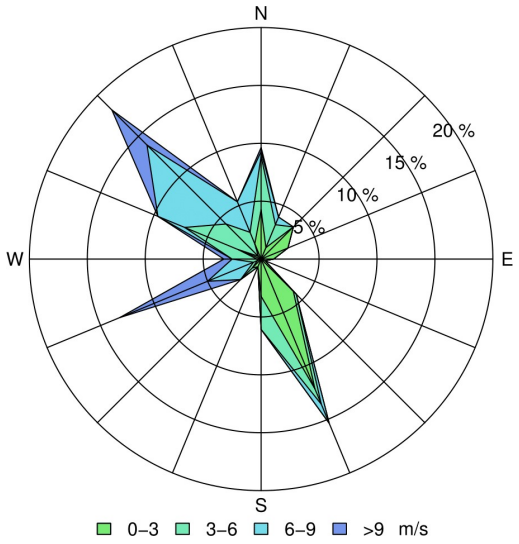

Figure 5.12. Wind rose for the isotope peak period 2 (IP2) from 01 to 12 January 2016. The circles illustrate relative frequencies from 5% to 20% of wind directions at certain wind speeds at 3 m above ground surface, respectively. A set of four colors is used for different classes of wind speeds in m/s as shown in the legend. Dominant wind directions are NW, SSE, WSW, and N.

Relative and specific humidity have maxima on 04 and 05 January with 94.6% (relative humidity at 2 m above ground surface) and 3.3 g/kg (specific humidity at 5 m above ground surface).

Ground surface

Snow height is mainly at and around the mean of 15.5 cm. But on 03 and 04 January a short increase up to 21.8 cm occurred, as shown in Figure A.5.

Soil

In Figure A.5, soil temperature at 1 cm below ground surface shows a similar trend to that of air temperature and decreases from 05 to 09 January before an increase follows. Soil liquid volumetric water content at 8 cm below ground surface only shows slight variations with a range of 1.7% around its mean of 5.7%.

5.3.3 Isotope peak period 3 (IP3)

With a duration of 19 days, the isotope peak period 3 (IP3) lasted from 18 March 2016 to 05 May 2016.

Water vapor isotopic composition

During the IP3, mean δ values are -42.1‰ (δ^{18}O) and -307.3‰ (δD). With diurnal fluctuations both δ^{18}O and δD increase from 18 March to peaks on 23 March with maxima of -33.0‰ (δ^{18}O) and -244.0‰ (δD). Afterwards, δ^{18}O and δD decrease until the end of the IP3 on 05 May 2016, as shown in Figure A.6. *d* has a mean of 29.1‰ during the IP3 and is nearly steady until it increases on 27 March and stays at higher values up to 49.9‰ until the end of the IP3. Concerning δD-δ^{18}O correlation, a slope of 6.8 and a δD-intercept of -22.5‰ has been observed, as shown in Figure 13.

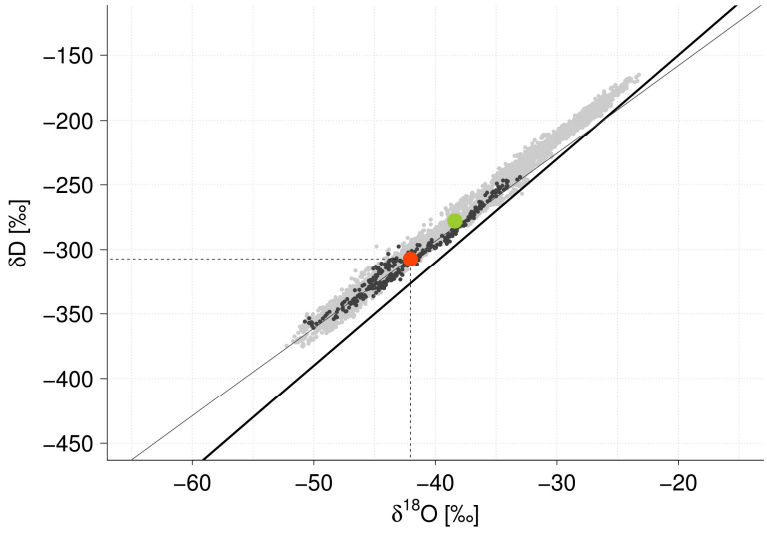

Figure 5.13. δD-δ^{18}O scatter plot for the isotope peak period 3 (IP3) from 18 March to 05 May 2016. Gray data points are those of all data from 01 July 2015 to 30 June 2016, black ones are those of the period. The thick line represents the GMWL ($\delta D = 8.0 \cdot \delta^{18}O + 10.0$), the thin line is the linear regression ($\delta D = 6.8 \cdot \delta^{18}O - 22.5$) with a coefficient of determination of $r^2 = 0.97$. Annual mean of δ^{18}O (-38.4‰) and δD (-277.8‰) is indicated by the green point, whereas the red point represents the periodic mean of δ^{18}O (-42.1‰) and δD (-307.3‰). Annual mean *d* is 29.3‰, periodic mean is 29.1‰.

Radiation

In Figure A.6, daily maxima of short-wave radiation (incoming and outgoing) constantly increase. Outgoing long-wave radiation has minima as incoming short-wave radiation peaks. The absolute minimum is reached on 23 March. Net radiation shows strong diurnal fluctuations with variations similar to incoming long-wave radiation from 18 to 23 March.

Air

Air temperature at 2 m above ground surface increases up to two peaks on 22 and 23 March with a maximum of -4.5 °C compared to the period mean of -20.7 °C. Atmospheric pressure has two minima in Figure A.6, as air temperature peaks. Both are below 101.3 kPa and therefore peaks of low-pressure. Two dominant wind directions are SE to S with a maximum on SSE, and WSW to NNW with a maximum on NW. Strongest winds with speeds up to 12.2 m/s were recorded between 18 and 24 March.

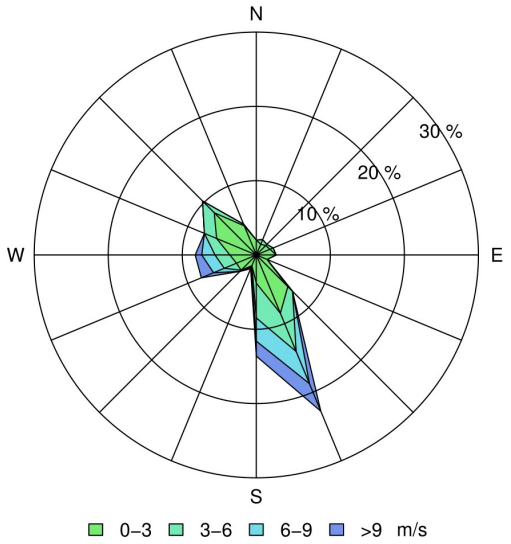

Figure 5.14. Wind rose for the isotope peak period 3 (IP3) from 18 March to 05 May 2016. The circles illustrate relative frequencies from 10% to 30% of wind directions at certain wind speeds at 3 m above ground surface, respectively. A set of four colors is used for different classes of wind speeds in m/s as shown in the legend. Dominant wind directions are SSE and NW.

As wind speed increases, both relative and specific humidity show peaks with values up to 95.6% (relative humidity at 2 m above ground surface) and 3.5 g/kg (specific humidity at 5 m above ground surface) in Figure A.6.

Ground surface

The mean snow height is 22.8 cm. Liquid precipitation was not recorded.

Soil

The trend of soil temperature at 1 cm below ground surface is similar to that of air temperature in Figure A.6 but with less strong peaks and a generally smoother curve shape. Its maximum is on 24 March. Soil liquid volumetric water content at 8 cm below ground surface only shows slight variations at a range of 1.7% around its mean of 5.5%.

5.3.4 Isotope peak period 4 (IP4)

The isotope peak period 4 (IP4) went from 23 April 2016 to 01 May 2016 and thus lasted nine days. During this period, $\delta^{18}O$ and δD have their highest peaks during deep winter.

Water vapor isotopic composition

During the IP4, mean δ values are -37.1‰ ($\delta^{18}O$) and -266.6‰ (δD). $\delta^{18}O$ and δD increase rapidly in Figure A.7 from 23 April within four days to maxima of -27.4‰ ($\delta^{18}O$) and -201.0‰ (δD) on 27 April. After that, both values again decrease with a similar slope. *d* has a mean of 30.4‰ and shows an opposite trend to that of $\delta^{18}O$ and δD in Figure A.7, but with another peak on 29 April with a maximum of 46.6‰. Concerning δD-$\delta^{18}O$ correlation, a slope of 6.0 and a δD-intercept of -20.9‰ has been observed, as shown in Figure 5.15.

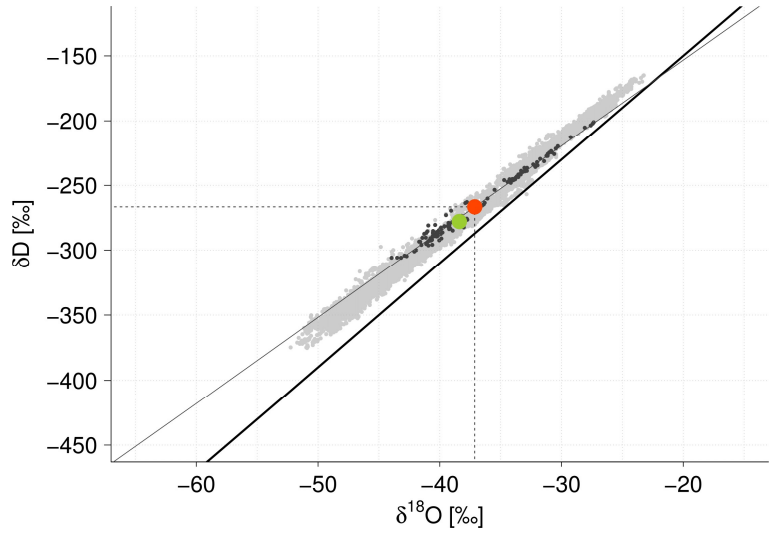

Figure 5.15. δD-$\delta^{18}O$ scatter plot for the isotope peak period 4 (IP4) from 23 April to 01 May 2016. Gray data points are those of all data from 01 July 2015 to 30 June 2016, black ones are those of the period. The thick line represents the GMWL ($\delta D = 8.0 \cdot \delta^{18}O + 10.0$), the thin line is the linear regression ($\delta D = 6.0 \cdot \delta^{18}O - 20.9$) with a coefficient of determination of $r^2 = 0.99$. Annual mean of $\delta^{18}O$ (-38.4‰) and δD (-277.8‰) is indicated by the green point, whereas the red point represents the periodic mean of $\delta^{18}O$ (-37.1‰) and δD (-266.6‰). Annual mean *d* is 29.3‰, periodic mean is 30.4‰.

Radiation

The curves of both in and out short-wave radiation in Figure A.7 are sinus-shaped from 23 to 24 April. From the next day on, both strongly change their curve shape and have lower daily maxima, especially during 25 and 27 April. At the same time, absolute values of long-wave radiation are both increasing. The maxima were recorded on 26 April (outgoing) and 25 April (incoming). Net radiation has its maximum on 23 April and its minimum on 29 April.

Air

Air temperature at depths of 2 m above ground surface trends are similar to that of incoming long-wave radiation and reaches its maximum of 0.7 °C on 26 April. After that it decreases, before another peak on 29 April was recorded, as shown in Figure A.7. Atmospheric pressure is decreasing during the IP4. On 28 April, it drops below 101.3 kPa and is therefore defined to be low-pressure from that day on. The average wind direction at 3 m above ground surface is WNW to NNW with wind speeds up to 10.0 m/s. The highest wind speed occurs from 25 to 27 April.

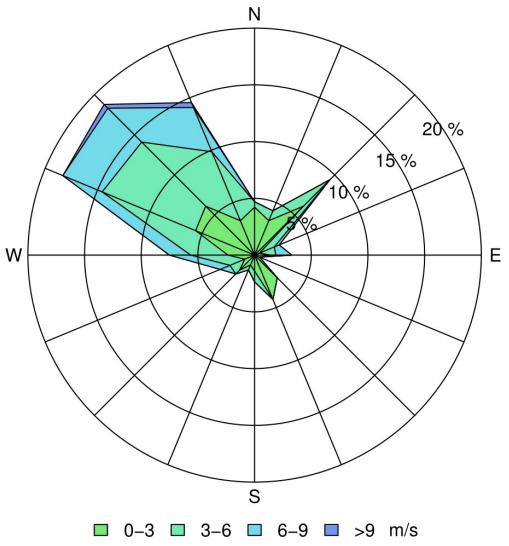

Figure 5.16. Wind rose for the isotope peak period 4 (IP4) from 23 April to 01 May 2016. The circles illustrate relative frequencies from 5% to 20% of wind directions at certain wind speeds at 3 m above ground surface, respectively. A set of four colors is used for different classes of wind speeds in m/s as shown in the legend. The dominant wind direction is WNW to NNW.

Specific humidity at 5 m above ground surface shows a similar curve shape to incoming short-wave radiation and air temperature in Figure A.7, with its maximum of 5.1 g/kg on 25 April and a decrease from that peak on until a mostly constant value is reached from 29 April on. Relative humidity at 2 m above ground surface shows similar trends over the entire period but

with less strong in- and decrease, but with a strong and short negative peak on 29 April with a value of 63.5%.

Ground surface

Liquid precipitation was recorded on 26 April, as shown in Figure A.7, with a total sum of 4.8 mm. It is the only record of liquid precipitation during deep winter (22 October 2015 to 14 May 2016). Snow depth decreases for 2.1 cm from that day on.

Soil

Soil temperature at 1 cm below ground surface shows a strong peak on the day of recorded liquid precipitation in Figure A.7. With a maximum of -2.2 °C on that day it is close to the freezing point, whereas before it was at and around -15 °C. Soil liquid volumetric water content at 8 cm below ground surface only shows slight variations at a range of 1.6% around its mean value of 5.8% in Figure A.7.

5.4 Linear correlations of isotopic composition with meteorological parameters

The Pearson correlation coefficient (r) of all meteorological and soil parameters with every isotope parameter was calculated for winter and the winter onset period (WOP), winter termination period (WTP), and isotope peak period (IP1 to IP4), respectively.

During winter (from 23 September 2015 to 15 June 2016), the strongest correlation is observed between specific humidity and both $\delta^{18}O$ ($r = 0.64$) and δD ($r = 0.66$). For $\delta^{18}O$ and δD, other relatively high correlations (defined as $r \geq 0.5$ for absolute r) exist with incoming long-wave radiation, outgoing long-wave radiation, and air temperature at 2 m above ground surface, as shown in Table 5.3.

For d only weak correlations during the overall winter period were calculated. According to absolute values, the strongest correlation exists with specific humidity ($r = -0.26$), as shown in Table 5.3. The correlation of d with air temperature ($r = -0.25$) is very similar to humidity. Generally, signs of r are opposite to those of $\delta^{18}O$ and δD.

For air temperature and specific humidity, absolute r with δ values and d increase in the course of the year, as the values from the WOP (21 September to 21 October 2015) to the WTP (23 April to 21 June 2016) over the isotope peak periods show in Table 5.3. This trend is also observed for absolute r between long-wave radiation in and out and d, respectively, whereas r

between long-wave radiation in and out and δ values fluctuate. During the IP2, inverse correlations of meteorological parameters with δ values and d are in contrast to the correlations between these parameters during the residual periods and the entire year, as shown in Table 5.3.

Table 5.3. Correlation coefficients (r) of meteorological with isotope parameters. Meteorological parameters are incoming long-wave radiation (*LWi*), outgoing long-wave radiation (*LWo*), air temperature at 2 m above ground surface (*Tair*), and specific humidity at 5 m above ground surface (*Hsp*). Isotope parameters are δ^{18}O, δD, and d. For winter only parameters with $r > 0.5$ or $r < -0.5$ to δ^{18}O and δD are displayed. For the winter onset period (WOP), winter termination period (WTP), and isotope peak periods 1 to 4 (IP1 to IP4), r between these parameters and isotope parameters are displayed without a threshold.

	Winter	**WOP**	**WTP**	**IP1**	**IP2**	**IP3**	**IP4**
	23 Sep 2015 to 15 Jun 2016	21 Sep 2015 to 21 Oct 2015	15 May 2016 to 21 Jun 2016	07 Nov 2015 to 01 Dec 2015	01 Jan 2016 to 12 Jan 2016	18 Mar 2016 to 05 Apr 2016	23 Apr 2016 to 01 May 2016
	δ^{18}O	**δ^{18}O**	**δ^{18}O**	**δ^{18}O**	**δ^{18}O**	**δ^{18}O**	**δ^{18}O**
LWi	0.58	0.60	0.74	0.40	-0.72	0.41	0.56
LWo	-0.60	-0.71	-0.75	-0.41	0.65	-0.58	-0.79
Tair	0.58	0.72	0.75	0.41	-0.65	0.62	0.80
Hsp	0.64	0.68	0.80	0.47	-0.50	0.68	0.76
	δD	**δD**	**δD**	**δD**	**δD**	**δD**	**δD**
LWi	0.59	0.61	0.72	0.43	-0.72	0.36	0.51
LWo	-0.62	-0.72	-0.74	-0.45	0.67	-0.53	-0.80
Tair	0.59	0.74	0.73	0.44	-0.67	0.56	0.80
Hsp	0.66	0.69	0.77	0.50	-0.51	0.64	0.76
	d	***d***	***d***	***d***	***d***	***d***	***d***
LWi	-0.25	-0.10	-0.71	-0.12	0.54	-0.50	-0.66
LWo	0.24	0.10	0.68	0.13	-0.40	0.60	0.65
Tair	-0.25	-0.08	-0.72	-0.13	0.38	-0.66	-0.66
Hsp	-0.26	-0.16	-0.84	-0.20	0.35	-0.62	-0.65

6 Discussion

Many fluctuations of water vapor isotopic composition are similar to those of meteorological and soil parameters during winter, as described above. In the following, numerical and graphical analyzes are interpreted.

6.1 Influences on water vapor isotopic composition

All in all, humidity (specific humidity) and temperature (long-wave radiation, air temperature) are the parameters that affect both δ values the most, while $\delta^{18}O$ and δD have practically the same r with each of them, as shown in Table 5.3.

6.1.1 Air temperature and humidity

Air temperature and humidity are strongly interlinked due to the temperature dependency of saturation vapor pressure: the higher the temperature the more humidity can be absorbed by air (Schönwiese, 2008). Due to a low mean air temperature during winter (-18.6 °C), specific humidity drops strongly and an extremely dry atmosphere with a mean of 1.4 g/kg is observed, as shown in Figure A.1.

With $r = 0.64$ for $\delta^{18}O$ and $r = 0.66$ for δD, specific humidity is the meteorological parameter most correlating with both δ values. Comparing the curves of specific humidity with $\delta^{18}O$ and δD in Figures A.1 to A.7, high similarities are visible. The increase of $\delta^{18}O$ and δD during the IP1 (Figure A.4), IP3 (Figure A.6), and IP4 (Figure A.7) goes along with an increase of specific humidity. In contrast, the trends of δ values during the IP2 (01 to 12 January 2016) in Figure A.5 anticorrelate with humidity with $r = -0.50$ ($\delta^{18}O$) and $r = -0.51$ (δD). This means, that fluctuations of isotopic δ values are not always controlled by humidity changes, but other processes, like moisture source changes, supported by wind direction and speed changes (Steen-Larsen et al., 2013). During the IP2, mean specific humidity (0.8 g/kg) and mean d (18.3‰) are the lowest compared to the residual isotope peak periods, respectively. This speaks for a local moisture source, as moisture from distant sources must always go along with an increase of the humidity level, as it is very low during winter on Samoylov Island (mean of 1.4 g/kg).

Air temperature is with $r = 0.58$ for $\delta^{18}O$ and $r = 0.59$ for δD the second most correlating meteorological parameter with both δ values in winter. During the IP4, the strongest correlation is observed with $r = 0.80$ for $\delta^{18}O$ and $\delta^{18}O$, respectively. Additionally, the only liquid precipitation during deep winter (22 October 2015 to 14 May 2016) was recorded during the IP4 on 26 April 2016, as shown in Figure A.7. An intensive cloud cover can be interpreted due to high values of incoming long-wave radiation and the decrease of incoming short-wave radiation the

day before and after the liquid precipitation event. Additionally, strong winds from NW occurred. During the cloud coverage and the strong winds, air temperature at 2 m above ground surface increase strongly up to 0.7 °C. Either warm air masses were brought to the field side from NW by convection as the strong winds imply or the cloud cover led to a local greenhouse effect. As absolute values of short-wave radiation both increase (solar radiation increases), absolute values of outgoing short-wave radiation does not increase on the day after the precipitation record compared to the day before (no change in albedo), incoming long-wave radiation decreases (cloud cover decreases), and the snow depth drop by 2.1 cm on the day of the liquid precipitation record, it can be interpreted as a snow melt event instead of rainfall. As a result of the increasing air temperature, specific humidity and both $\delta^{18}O$ and δD increases.

High *d* for all data from 01 July 2015 to 30 June 2016 (29.3‰) and every examined period (18.3‰ to 32.0‰) could indicate low humidity levels at the vapor source region (Clark and Fritz, 1997). But as *d* of liquid precipitation from Tiksi, Siberia, which is 115 km away from Samoylov Island, has a mean of 3.4‰ and a range from -15.2‰ to 16.5‰ for monthly means from October 2003 to August 2007 (Kloss, 2008), the high *d* for Samoylov Island must be due to long distance transport of the moisture, as with every re-evaporation *d* increases.

Absolute correlations between air temperature and *d* and specific humidity and *d* increase with every isotope peak period from -0.13 (air temperature) and -0.20 (specific humidity) during the IP1 to -0.66 (air temperature) and -0.65 (specific humidity) during the IP4, which speaks for the increase of local moisture sources, as an increase of air temperature and specific humidity would lead to a decrease of *d* if a strong anticorreation exists.

6.1.2 Long-wave radiation

Outgoing long-wave radiation strongly anti-correlates with $\delta^{18}O$ and δD, respectively. Due to polar night, long-wave radiation, emitted by the earth and reflected by clouds and aerosols in the atmosphere (Kiehl and Trenberth, 1997), is the only source of (thermal) radiation during winter. Thus, its intensity strongly drives local air temperature, which is obvious due to correlations of $r = 0.93$ between incoming long-wave radiation and air temperature at 2 am above the ground surface, and $r = -0.99$ between outgoing long-wave radiation and air temperature. This strong correlation is also visible by comparing curve shapes of long-wave radiation with air temperature in Figures A.1 to A.7. An increase of absolute values of long-wave radiation goes along with an increase of air temperature during all isotope peak periods. The strong correlation between isotopic δ values and long-wave radiation is due to this relation, as isotope fractionation is sensitive to air temperature (Clark and Fritz, 1997).

6.2 Winter onset and termination periods

During the winter onset period (WOP, from 21 September to 21 October 2015) and winter termination period (WTP, from 15 May to 21 June 2016), absolute *r* differ from those of the entire winter concerning *d*, as shown in Table 5.3. *d* has even lower absolute *r* during the WOP (-0.08 with air temperature, -0.16 with specific humidity), but very high absolute *r* during the WTP (-0.72 with air temperature, -0.84 with specific humidity). This could be interpreted as the domination of distant moisture sources during the WOP, as parameters, that affect local moisture (air temperature and specific humidity) have a weak correlation with *d*, available liquid water sources freeze (Molo Lake on 29 September, Lena River on 07 October 2015), and snow accumulates on 21 September 2015. Whereas during the WTP strong correlations between air temperature, specific humidity, and *d*, respectively, are observed. This speaks for local affection of *d* and thus for a local isotope signature, corroborated by the fact, that the WTP has the highest mean air temperature (0.4 °C) compared to every other period and thus shows favorable conditions of local moisture formation.

The interrelated processes during the WOP lead to freezing of most available liquid water, except for the deeper lakes, which remain unfrozen under an up to 2 m thick ice cover (Boike et al., 2015). Thus, local sources of water vapor are limited during winter. Evaporation is replaced by sublimation, which is the major local process of water vapor formation (Liston and Sturm, 2004), though it is the most energy-intensive phase change (Schönwiese, 2008) during a time of dominated negative net radiation. Due to polar night from 20 November 2015 to 26 January 2016, incoming short-wave radiation equals zero, as shown in Figure A.1. The remaining emission of long-wave radiation from the earth leads to an energy deficit, visible through a decreasing soil temperature during winter in Figure A.1, though clouds and aerosols in the atmosphere are reflectors (Kiehl and Trenberth, 1997), so that the incoming component is a major source of energy during winter. Additionally, strong winds are a decisive source of (kinetic) energy, which increase the rate of sublimation (Schmidt, 1972), as explained in chapter 2.1. Apart from sublimation, only advection that brings moisture from distant origins is another source of water vapor during winter (Steen-Larsen et al., 2013). During the IP1 (from 07 November to 01 December 2015, Figure A.4), IP3 (from 18 March to 05 April 2016, Figure A.6), and IP4 (from 23 April to 01 May, Figure A.7), peaks of both $\delta^{18}O$ and δD go along with strong winds, which can be interpreted as either synoptic air movements bringing water vapor from distant origins or as conditions for an increased sublimation rate after Schmidt (1972).

6.3 δD-δ^{18}O correlation

Table 6.1. Statistical values of all δD-δ^{18}O scatter plots. With respective mean of δD, δ^{18}O, and *d*, along with slope, intercept, and coefficient of determination (r^2) of the linear regressions for all data, the winter onset period (WOP), winter termination period (WTP), and isotope peak periods 1 to 4 (IP1 to IP4).

	All data	WOP	WTP	IP1	IP2	IP3	IP4
	01 Jul 2015 to 30 Jun 2016	21 Sep 2015 to 21 Oct 2015	15 May 2016 to 21 Jun 2016	07 Nov 2015 to 01 Dec 2015	01 Jan 2016 to 12 Jan 2016	18 Mar 2016 to 05 Apr 2016	23 Apr 2016 to 01 May 2016
δD [‰]	-277.8	-235.0	-261.2	-292.5	-272.3	-307.3	-266.6
δ^{18}O [‰]	-38.4	-33.4	-33.4	-39.8	-36.3	-42.1	-37.1
d [‰]	29.3	32.4	25.3	25.9	18.3	29.1	30.4
Slope	7.4	7.1	7.1	7.0	6.9	6.8	6.6
Intercept	7.7	2.2	-8.3	-12.0	-22.5	-22.5	-20.9
r^2	0.99	0.98	0.99	1.00	0.99	0.97	0.99

With mean values of -38.4‰ (δ^{18}O) and -277.8‰ (δD) for all data, the examined vapor is strongly depleted in heavy isotopes compared to ocean water (*i.e.* VSMOW). But as shown in Figure 2.2, these low values are in the expected range for cold climate and high latitudes, which is corresponding to the conditions of the field site. As air is transported poleward, a constant decrease of both δ^{18}O and δD occur due to removal of ^{18}O and D (Bonne et al., 2014).

The wide range of data points in the δD-δ^{18}O scatter plot in Figure 5.1 for all data from 01 July 2015 to 30 June 2016 is due to the wide range of air temperature, as both δ^{18}O and δD strongly depend on temperature (Clark and Fritz, 1997, Bastrikov et al., 2014, Bonne et al., 2014).

The slope of the linear regression of the same plot equals 7.4 (Table 6.2), hence only slightly lower than of the GMWL, which has a slope of 8. This indicates the contribution of kinetic fractionation processes, *i.e.* from local vapor sources (Clark and Fritz, 1997). The slope of 7.4 is very similar to the slope of 7.57, which has been observed by Kloss (2008) for liquid precipitation in Tiksi, Siberia (115 km away from Samoylov Island). Also the slope of 7.5 observed in western Siberia by Bastrikov et al. (2014) is very similar, though geographical conditions differ. Bonne et al. (2013) reported a slope of 6.8 for data monitored in southern Greenland.

The slopes decrease during winter from 7.0 (IP1) to 6.6 (IP4), as the values of the isotope peak periods show in Table 6.2. All are below the global mean of 8 but never below 6.6, which speaks for a substantial (potentially increasing) contribution of local vapor sources and re-evaporation (Clark and Fritz, 1997) during winter.

7 Conclusions

The aim of this thesis was to identify correlations of land and atmosphere processes with water vapor isotopic composition at a field site in Northern Siberia during winter, which was defined by the presence of snow (23 September 2015 to 15 May 2016). For this purpose, one year of data from 01 July 2015 to 30 June 2016 including meteorological, soil, and isotope parameters ($\delta^{18}O$, δD, and d) were analyzed.

Generally, both $\delta^{18}O$ and δD are very low during winter, with means of -41.3‰ for $\delta^{18}O$ and -299.6‰ for δD. But large ranges of $\delta^{18}O$ and δD were especially observed during four periods of long-term peaks with δ values up to -27.4‰ for $\delta^{18}O$ and -201.0‰ for δD on 27 April 2016. It was detected that specific humidity ($r = 0.64$ with $\delta^{18}O$, $r = 0.66$ with δD) and air temperature ($r = 0.58$ with $\delta^{18}O$, $r = 0.59$ with δD) have a distinct correlation with both δ values during winter, as expected from results of many publications (*e.g.* Bastrikov et al., 2014, Bonne et al, 2014, Masson-Delmotte et al., 2015). Thus, the variability of δ values is mostly caused by changes of local air temperatures and humidity levels.

Surprisingly, both δ values anticorrelate with air temperature ($r = -0.65$ with $\delta^{18}O$, $r = -0.67$ with δD) and specific humidity ($r = -0.50$ with $\delta^{18}O$, $r = -0.51$ with δD) during a period (01 to 12 January 2016) of increasing δ values in winter. This means that fluctuations of isotopic δ values are not solely controlled by air temperature and humidity changes, but other processes, like moisture source changes, supported by wind direction and speed changes come into play (Steen-Larsen et al., 2013). During this period, mean specific humidity (0.8 g/kg) and mean d (18.3‰) are the lowest compared to the residual isotope peak periods, respectively. This speaks for a local moisture source, as moisture from distant sources must always go along with an increase of the humidity level, as it is very low during winter on Samoylov Island (mean of 1.4 g/kg).

With the beginning of winter, processes that affect the phase changes between liquid water, ice, and vapor occur, and snow accumulates. Thus, sublimation is the only local process that involves the formation of moisture during winter. With 29.3‰, a high mean of d during the entire year was identified to provide information about low humidity conditions and strong kinetic fractionation at evaporation and sublimation at the moisture source location. Additionally, the strongest correlation exists with specific humidity ($r = -0.26$). After Schmidt (1972), a low humidity level increases the sublimation rate. This corroborates the observed anticorrelation between d and specific humidity, as d is sensitive to re-evaporation, *i.e.* sublimation of ice and snow.

A wide range of data points in the δD-δ^{18}O scatter plots for the overall year is due to the wide range of air temperatures, as both δ^{18}O and δD strongly depend on temperature (Clark and Fritz, 1997, Bastrikov et al., 2014, Bonne et al., 2014). The slope of 7.4 of the regression line indicates a contribution of secondary fractionation processes, *i.e.* from local vapor sources. Slopes of linear regressions of δD-δ^{18}O scatter plots for the isotope peak periods decrease during winter from 7.0 (IP1, 07 November to 01 December 2015) to 6.6 (IP4, 23 April to 01 May 2016), which indicates local moisture sources also during winter.

Limitations of this thesis are the short time period of the data considered, data gaps, simple numerical and graphical examinations, and the restricted extent. By comparing water vapor isotopic composition between different years, a more precise interpretation of correlations with land and atmosphere processes could be possible. The application of a numerical model, as often done in literature, could improve the analyses of environmental situations during the examined periods. And above all, the extensive data set provides much more information and scope for exploring the correlations of land and atmosphere processes with water vapor isotope composition than is presented in this thesis.

References

ACIA. (2004). Impacts of a Warming Arctic: Arctic Climate Impact Assessment. Cambridge University Press.

Alfred-Wegener-Institute, Helmholtz-Center for Polar and Marchine Research. (2015, October 20). Research Station "Samoylov Island". Retrieved from http://www.awi.de/en/expedition/stations/island-samoylov.html

Bastrikov, V., Steen-Larsen, H. C., Masson-Delmotte, V., Gribanov, K., Cattani, O., Jouzel, J., and Zakharov, V. (2014). Continuous measurements of atmospheric water vapour isotopes in western Siberia (Kourovka). *Atmospheric Measurement Techniques*, 7(6), 1763–1776.

Boike, J., Kattenstroth, B., Abramova, Ekaterina, Bornemann, N., Chetverova, A., Fedorova, I., Fröb, K., Grigoriev, Mikhail, Grüber, M., Kutzbach, Lars, Langer, M., Minke, M., Muster, S., Piel, K., Pfeiffer, Eva-Marchia, Stoof, G., Westermann, S., Wischnewski, K., Wille, C., and Hubberten, H.-W. (2013). Baseline characteristics of climate, permafrost and land cover from a new permafrost observatory in the Lena River Delta, Siberia (1998–2011). *Biogeosciences*, 10(3), 2105–2128.

Boike, J., Georgi, C., Kirilin, G., Muster, S., Abramova, K., Fedorova, I., Chetverova, A., Grigoriev, M., Bornemann, N., and Langer, M. (2015). Thermal processes of thermokarst lakes in the continuous permafrost zone of northern Siberia–observations and modeling (Lena River Delta, Siberia). *Biogeosciences*, 12(20), 5941–5965.

Bonne, J. L., Masson-Delmotte, V., Cattani, O., Delmotte, M., Risi, C., Sodemann, H., and Steen-Larsen, H. C. (2014). The isotopic composition of water vapour and precipitation in Ivittuut, southern Greenland. *Atmospheric Chemistry and Physics*, 14(9), 4419–4439.

Bonne, J. L., Steen-Larsen, H. C., Risi, C., Werner, M., Sodemann, H., Lacour, J. L., Fettweis, X., Cesana, G., Delmotte, M., Cattani, O., Vallelonga, P., Kjær, H. A., Clerbaux, C., Sveinbjörnsdóttir, Á. E., and Masson-Delmotte, V. (2015). The summer 2012 Greenland heat wave: In situ and remote sensing observations of water vapor isotopic composition during an atmospheric river event. *Journal of Geophysical Research: Atmospheres*, 120(7), 2970–2989.

Bonne, J. L., Werner, M., Meyer, H., Kipfstuhl, S., Rabe, B., Behrens, M., Schönicke, L., Steen-Larsen, H. C., and Masson-Delmotte, V. (2016, April). Isotopes in the Arctic atmospheric water cycle. In *EGU General Assembly Conference Abstracts* (Vol. 18, p. 16983).

Bonne, J. L., Werner, M., Meyer, H., Kipfstuhl, S., Rabe, B., Behrens, M., and Schönicke, L. (2016, December). *Eastern Arctic water vapor isotopic signature*. Potsdam.

Brown, J., Ferrians Jr, O. J., Heginbottom, J. A., & Melnikov, E. S. (1997). *Circum-Arctic map of permafrost and ground-ice conditions*. Reston, VA: US Geological Survey.

Clark, I. D., and Fritz, P. (1997). *Environmental Isotopes in Hydrogeology*. CRC press.

Craig, H. (1961). Isotopic variations in meteoric waters. *Science*, 133(3465), 1702–1703.

Dansgaard, W. (1964). Stable isotopes in precipitation. *Tellus*, *16*(4), 436–468.

Dingman, S. L. (2015). *Physical Hydrology*. Waveland press.

Gorelick, N., Hancher, M., Dixon, M., Ilyushchenko, S., Thau, D., and Moore, R. (2017). Google Earth Engine: Planetary-scale geospatial analysis for everyone. *Remote Sensing of Environment*.

Guijarro, J. A. (2016). CLIMATOL (Version 3.0) [source code]. Retrieved from http://www.climatol.eu

Kiehl, J. T., and Trenberth, K. E. (1997). Earth's annual global mean energy budget. *Bulletin of the American Meteorological Society*, *78*(2), 197–208.

Kloss, A. L. (2008). *Water isotope geochemistry of recent precipitation in Central and North Siberia as a proxy for the local and regional climate system*. (Diploma Thesis). Leibniz Universität, Hannover, Germany.

Kurita, N. (2011). Origin of Arctic water vapor during the ice-growth season. *Geophysical Research Letters*, 38(2).

Liston, G. E., and Sturm, M. (2004). The role of winter sublimation in the Arctic moisture budget. *Hydrology Research*, 35(4–5), 325–334.

Masson-Delmotte, V., Steen-Larsen, H. C., Zanetti, N., Cattani, O., Maturilli, M., Debatin, S., Terzer, S., Bonne, J. L., and Schneider, M. (2015, April). Understanding climatic controls on Svalbard water vapour and precipitation isotopic composition. In *EGU General Assembly Conference Abstracts* (Vol. 17).

Merlivat, L., and Jouzel, J. (1979). Global climatic interpretation of the deuterium-oxygen 18 relationship for precipitation. *Journal of Geophysical Research: Oceans*, *84*(C8), 5029–5033.

Permafrost Subcommittee. (1988). Glossary of permafrost and related ground-ice terms. *Associate Committee on Geotechnical Research, National Research Council of Canada, Ottawa*, 156.

Popov, I. V., Micklin, P. P., Owen L. (2016, November 11). Lena River. Retrieved from http://www.britannica.com/place/lena-river

Riedel, E. (2010). *Allgemeine und Anorganische Chemie*. Walter de Gruyter.

SAHRA. (2005). Summary diagram of how hydrologic processes affect oxygen and hydrogen isotopic composition of water. Retrieved from http://web.sahra.arizona.edu/pro-grams/isotopes/oxygen.html

Schmidt Jr, R. A. (1972). Sublimation of wind-transported snow – a model. *USDA Forest Service research paper RM-United States, Rocky Mountain Forest and Range Experiment Station*.

Schönwiese, C. D. (2008): *Klimatologie*. Eugen Ulmer.

Steen-Larsen, H. C., Johnsen, S. J., Masson-Delmotte, V., Stenni, B., Risi, C., Sodemann, H., Balslev-Clausen, D., Blunier, T., Dahl-Jensen, D., Ellehøj, M. D., Falourd, S., Grindsted, A., Gkinis, V., Jouzel, J., Popp, T., Sheldon, S., Simonsen, S. B., Sjolte, J., Steffensen, J. P., Sperlich, P., Sveinbjörnsdóttir, A. E., Vinther, B. M., and White, J. W. C. (2013). Continuous monitoring of summer surface water vapor isotopic composition above the Greenland Ice Sheet. *Atmospheric Chemistry and Physics*, 13(9), 4815–4828.

Woo, M.-K. (2012). *Permafrost Hydrology*. Springer Science & Business Media.

Zhang, T., Barry, R. G., Knowles, K., Heginbottom, J. A., and Brown, J. (2008). Statistics and characteristics of permafrost and ground-ice distribution in the Northern Hemisphere. *Polar Geography*, 31(1–2), 47–68.

Acknowledgements

Thanks to everyone who supervised me during preparing and writing this thesis. It was a good experience and I learned a lot. In particular I would like to say thank you to the AWI for offering the chance to work with their data sets, SPARC for meteorological, soil, and waterbody data, and several discussions with the group, Julia Boike for many discussions and even more ideas, Hanno Meyer and Jean-Louis Bonne from Iso-Arc for isotope data and a wonderful support, for explaining isotope geochemistry well and often, and giving extensive feedback for plots and ideas, Axel Bronstert for the good discussion, Sofia Antonova for providing and explaining remote sensing data of the delta, Stephan Lange for providing scripts and help with R, Peter Schreiber for providing data and showing many details in the data, Christoph Georgi for providing lake data and an R script, and Sally Ann Jahn for checking my thesis draft.

Appendix A Time series plots

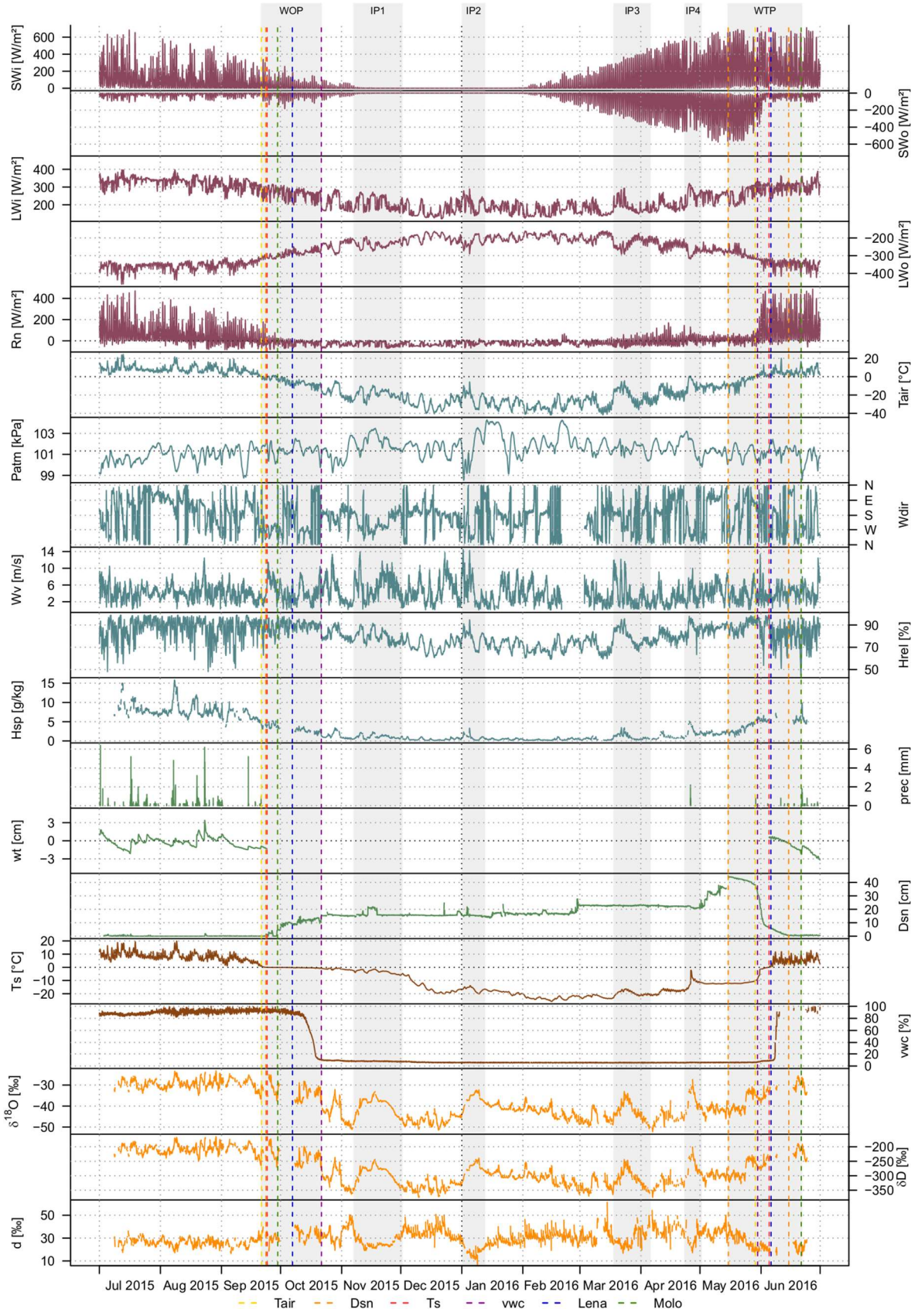

Figure A.1. Time series plot for all data from 01 July 2015 to 30 June 2016 with incoming short-wave radiation (*SWi*), outgoing short-wave radiation (*SWo*), incoming long-wave radiation (*LWi*), outgoing long-wave radiation

(*LWo*), net radiation (*Rn*), air temperature at 2 m above ground surface (*Tair*), atmospheric pressure (*Patm*), wind direction at 3 m above ground surface (*Wdir*), wind speed at 3 m above ground surface (*Wv*), relative humidity at 2 m above ground surface (*Hrel*), specific humidity at 5 m above ground surface (*Hsp*), liquid precipitation (*prec*), water table (*wt*), snow depth (*Dsn*), soil temperature at 1 cm below ground surface (*Ts*), soil liquid volumetric water content at 8 cm below ground surface (*vwc*), δ^{18}O, δD, and deuterium excess (*d*) from top to bottom. Gray bars illustrate all periods examined in this thesis: the winter onset period (WOP, 21 September to 21 October 2015), winter termination period (WTP, 15 May to 21 June 2016), isotope peak period 1 (IP1, 07 November to 01 December 2015), isotope peak period 2 (IP2, 01 to 12 January 2016), isotope peak period 3 (IP3, 18 March to 05 April 2016), and isotope peak period 4 (IP4, 23 April to 01 May 2016). Colorful dashed lines represent time points of environmental processes (found in Table 6.2) with each color representing one parameter as displayed in the legend and are shown in greater detail in Figures A.2 and A.3. Colors of the curves signalize the respective environmental group, as defined in this thesis: radiation (*SWi*, *SWo*, *LWi*, *LWo*, *Rn*), air (*Tair*, *Patm*, *Wdir*, *Wv*, *Hrel*, *Hsp*), ground surface (*prec*, *wt*, *Dsn*), soil (*Ts*, *vwc*), and water vapor isotopic composition (δ^{18}O, δD, *d*).

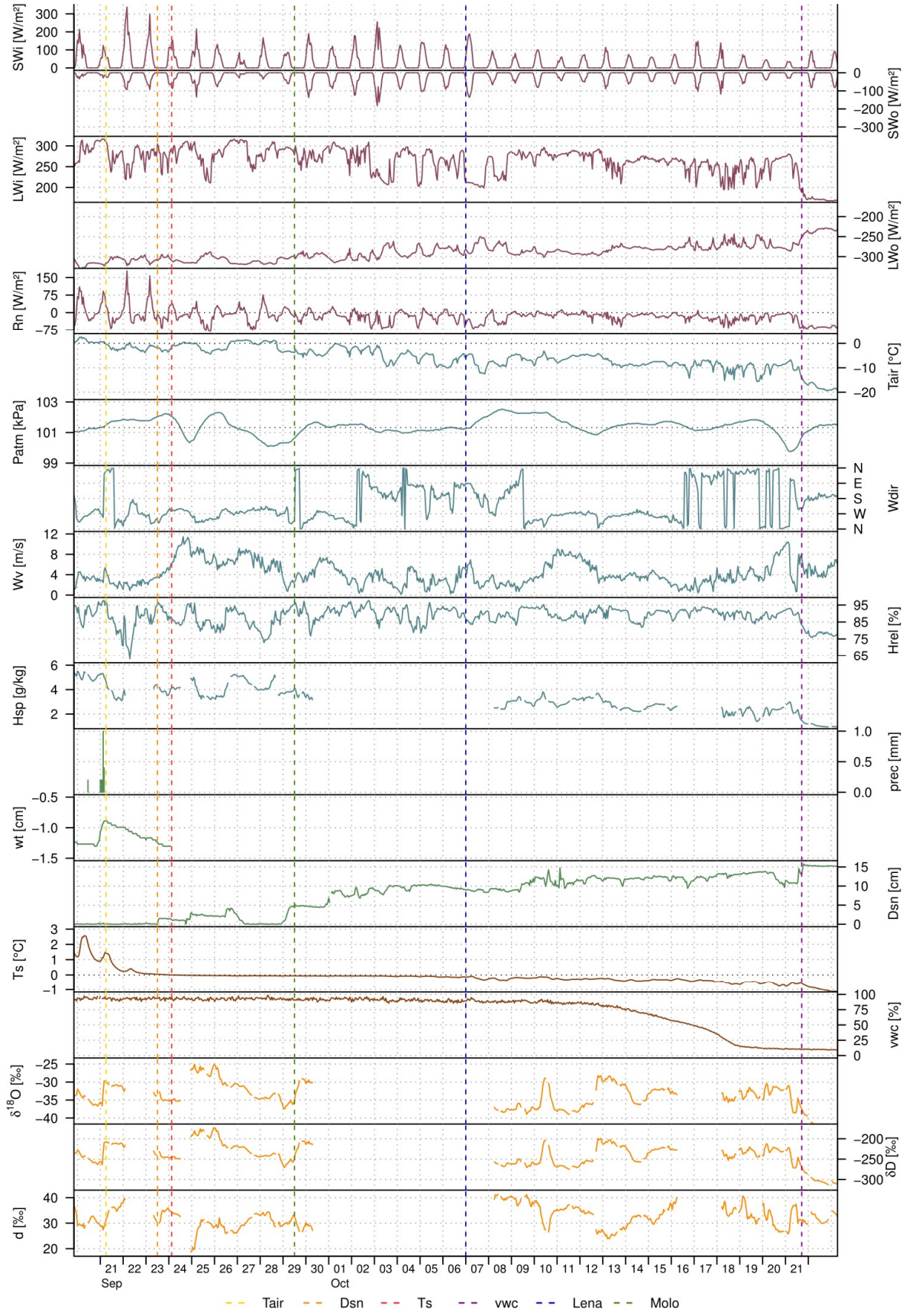

Figure A.2. Time series plot for the winter onset period (WOP) from 21 September to 21 October 2015 with incoming short-wave radiation (*SWi*), outgoing short-wave radiation (*SWo*), incoming long-wave radiation (*LWi*),

outgoing long-wave radiation (*LWo*), net radiation (*Rn*), air temperature at 2 m above ground surface (*Tair*), atmospheric pressure (*Patm*), wind direction at 3 m above ground surface (*Wdir*), wind speed at 3 m above ground surface (*Wv*), relative humidity at 2 m above ground surface (*Hrel*), specific humidity at 5 m above ground surface (*Hsp*), liquid precipitation (*prec*), water table (*wt*), snow depth (*Dsn*), soil temperature at 1 cm below ground surface (*Ts*), soil liquid volumetric water content at 8 cm below ground surface (*vwc*), δ^{18}O, δD, and deuterium excess (*d*) from top to bottom. Colorful dashed lines represent time points of environmental processes (found in Tables 5.1 and 5.2) with each color representing one parameter as displayed in the legend. These processes are chronologically: air temperature drops below 0 °C, soil temperature reaches 0 °C, first snow accumulates, the ice cover of Molo (lake) builds up, the Lena River freezes, and soil liquid volumetric water content reaches 0%. Colors of the curves signalize the respective environmental group, as defined in this thesis: radiation (*SWi*, *SWo*, *LWi*, *LWo*, *Rn*), air (*Tair*, *Patm*, *Wdir*, *Wv*, *Hrel*, *Hsp*), ground surface (*prec*, *wt*, *Dsn*), soil (*Ts*, *vwc*), and water vapor isotopic composition (δ^{18}O, δD, *d*).

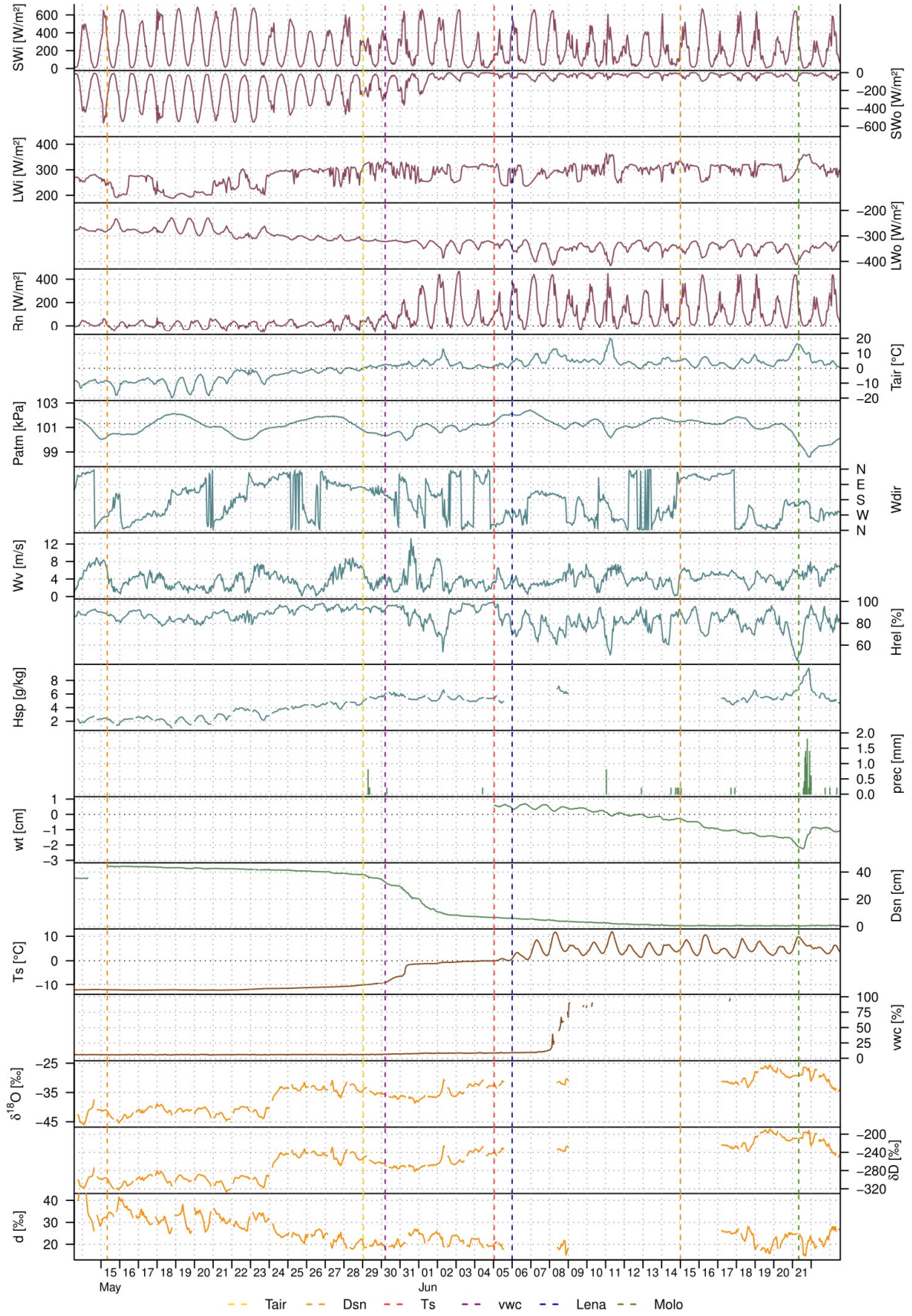

Figure A.3. Time series plot for the winter termination period (WTP) from 15 May to 21 June 2016 with incoming short-wave radiation (*SWi*), outgoing short-wave radiation (*SWo*), incoming long-wave radiation (*LWi*), outgoing long-wave radiation (*LWo*), net radiation (*Rn*), air temperature at 2 m above ground surface (*Tair*), atmospheric

pressure (*Patm*), wind direction at 3 m above ground surface (*Wdir*), wind speed at 3 m above ground surface (*Wv*), relative humidity at 2 m above ground surface (*Hrel*), specific humidity at 5 m above ground surface (*Hsp*), liquid precipitation (*prec*), water table (*wt*), snow depth (*Dsn*), soil temperature at 1 cm below ground surface (*Ts*), soil liquid volumetric water content at 8 cm below ground surface (*vwc*), $\delta^{18}O$, δD, and deuterium excess (*d*) from top to bottom. Colorful dashed lines represent time points of environmental processes (found in Table 6.2) with each color representing one parameter as displayed in the legend. These processes are chronologically: snow depth decreases, air temperature rises above 0 °C, soil liquid volumetric water content increases rapidly, soil temperature is above 0 °C, the ice cover of the Lena River breaks up, no snow is left, and Molo (lake) is ice free. Colors of the curves signalize the respective environmental group, as defined in this thesis: radiation (*SWi*, *SWo*, *LWi*, *LWo*, *Rn*), air (*Tair*, *Patm*, *Wdir*, *Wv*, *Hrel*, *Hsp*), ground surface (*prec*, *wt*, *Dsn*), soil (*Ts*, *vwc*), and water vapor isotopic composition ($\delta^{18}O$, δD, *d*).

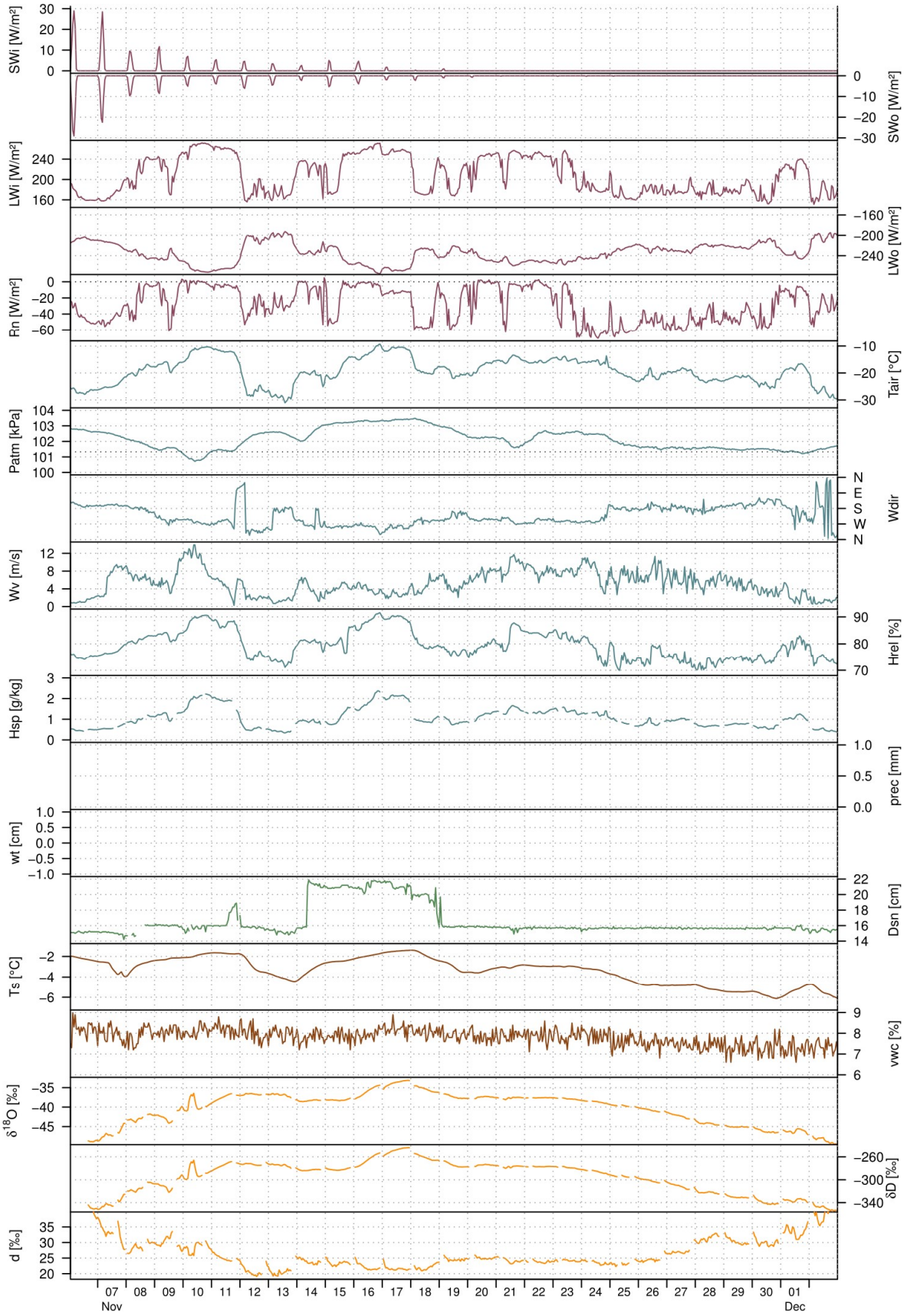

Figure A.4. Time series plot for the isotope peak period 1 (IP1) from 07 November to 01 December 2015 with incoming short-wave radiation (*SWi*), outgoing short-wave radiation (*SWo*), incoming long-wave radiation (*LWi*),

outgoing long-wave radiation (*LWo*), net radiation (*Rn*), air temperature at 2 m above ground surface (*Tair*), atmospheric pressure (*Patm*), wind direction at 3 m above ground surface (*Wdir*), wind speed at 3 m above ground surface (*Wv*), relative humidity at 2 m above ground surface (*Hrel*), specific humidity at 5 m above ground surface (*Hsp*), liquid precipitation (*prec*), water table (*wt*), snow depth (*Dsn*), soil temperature at 1 cm below ground surface (*Ts*), soil liquid volumetric water content at 8 cm below ground surface (*vwc*), $\delta^{18}O$, δD, and deuterium excess (*d*) from top to bottom. The maximum δ values are on 17 November 2015. Colors of the curves signalize the respective environmental group, as defined in this thesis: radiation (*SWi*, *SWo*, *LWi*, *LWo*, *Rn*), air (*Tair*, *Patm*, *Wdir*, *Wv*, *Hrel*, *Hsp*), ground surface (*prec*, *wt*, *Dsn*), soil (*Ts*, *vwc*), and water vapor isotopic composition ($\delta^{18}O$, δD, *d*).

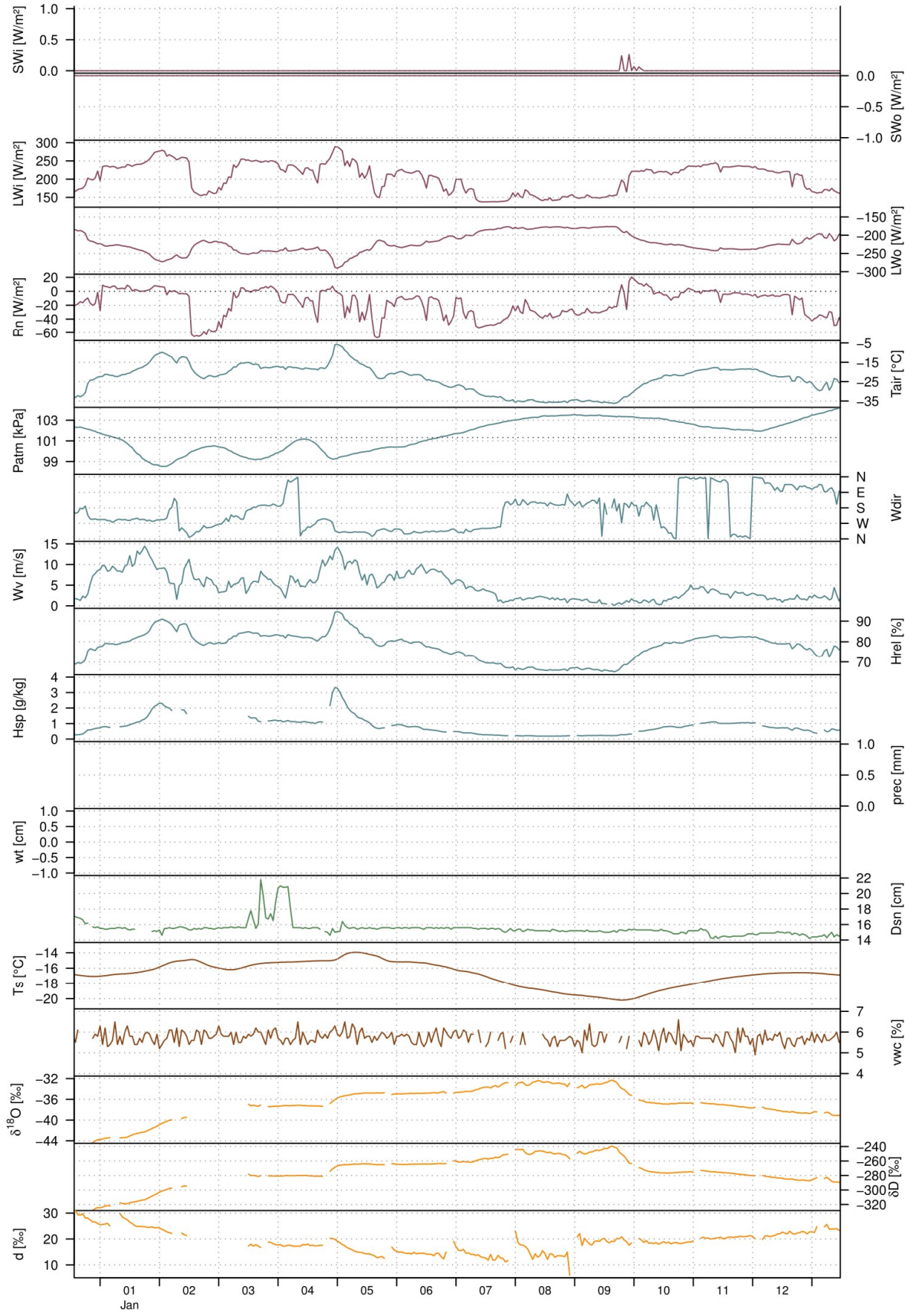

Figure A.5. Time series plot for the isotope peak period 2 (IP2) from 01 to 12 January 2016 with incoming short-wave radiation (*SWi*), outgoing short-wave radiation (*SWo*), incoming long-wave radiation (*LWi*), outgoing long-wave radiation (*LWo*), net radiation (*Rn*), air temperature at 2 m above ground surface (*Tair*), atmospheric pressure

(*Patm*), wind direction at 3 m above ground surface (*Wdir*), wind speed at 3 m above ground surface (*Wv*), relative humidity at 2 m above ground surface (*Hrel*), specific humidity at 5 m above ground surface (*Hsp*), liquid precipitation (*prec*), water table (*wt*), snow depth (*Dsn*), soil temperature at 1 cm below ground surface (*Ts*), soil liquid volumetric water content at 8 cm below ground surface (*vwc*), δ^{18}O, δD, and deuterium excess (*d*) from top to bottom. The maximum δ values are on 09 January 2016. Colors of the curves signalize the respective environmental group, as defined in this thesis: radiation (*SWi*, *SWo*, *LWi*, *LWo*, *Rn*), air (*Tair*, *Patm*, *Wdir*, *Wv*, *Hrel*, *Hsp*), ground surface (*prec*, *wt*, *Dsn*), soil (*Ts*, *vwc*), and water vapor isotopic composition (δ^{18}O, δD, *d*).

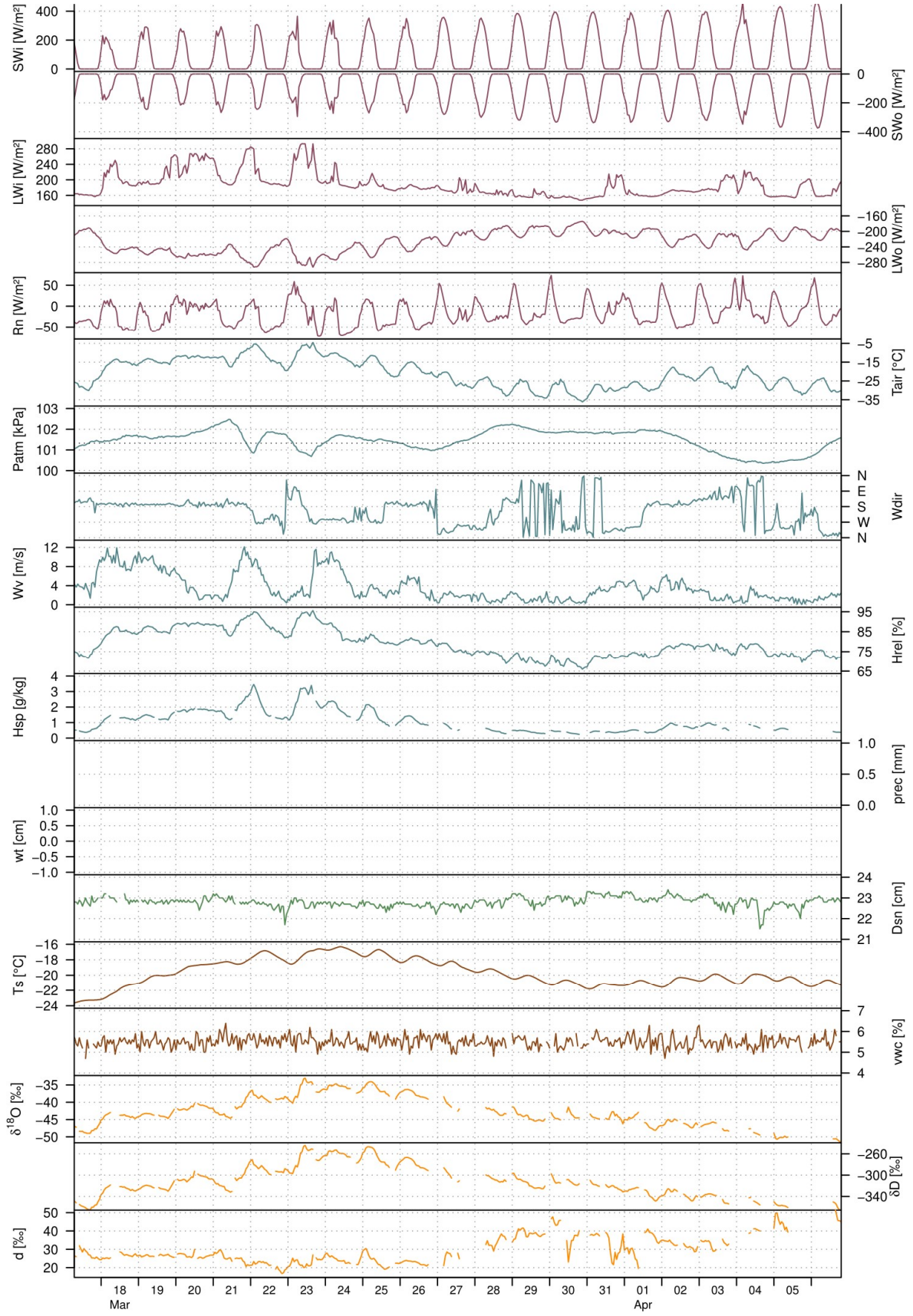

Figure A.6. Time series plot for the isotope peak period 3 (IP3) from 18 March to 05 Apr 2016 with incoming short-wave radiation (*SWi*), outgoing short-wave radiation (*SWo*), incoming long-wave radiation (*LWi*), outgoing long-wave radiation (*LWo*), net radiation (*Rn*), air temperature at 2 m above ground surface (*Tair*), atmospheric

pressure (*Patm*), wind direction at 3 m above ground surface (*Wdir*), wind speed at 3 m above ground surface (*Wv*), relative humidity at 2 m above ground surface (*Hrel*), specific humidity at 5 m above ground surface (*Hsp*), liquid precipitation (*prec*), water table (*wt*), snow depth (*Dsn*), soil temperature at 1 cm below ground surface (*Ts*), soil liquid volumetric water content at 8 cm below ground surface (*vwc*), δ^{18}O, δD, and deuterium excess (*d*) from top to bottom. The maximum δ values are on 23 March 2016. Colors of the curves signalize the respective environmental group, as defined in this thesis: radiation (*SWi*, *SWo*, *LWi*, *LWo*, *Rn*), air (*Tair*, *Patm*, *Wdir*, *Wv*, *Hrel*, *Hsp*), ground surface (*prec*, *wt*, *Dsn*), soil (*Ts*, *vwc*), and water vapor isotopic composition (δ^{18}O, δD, *d*).

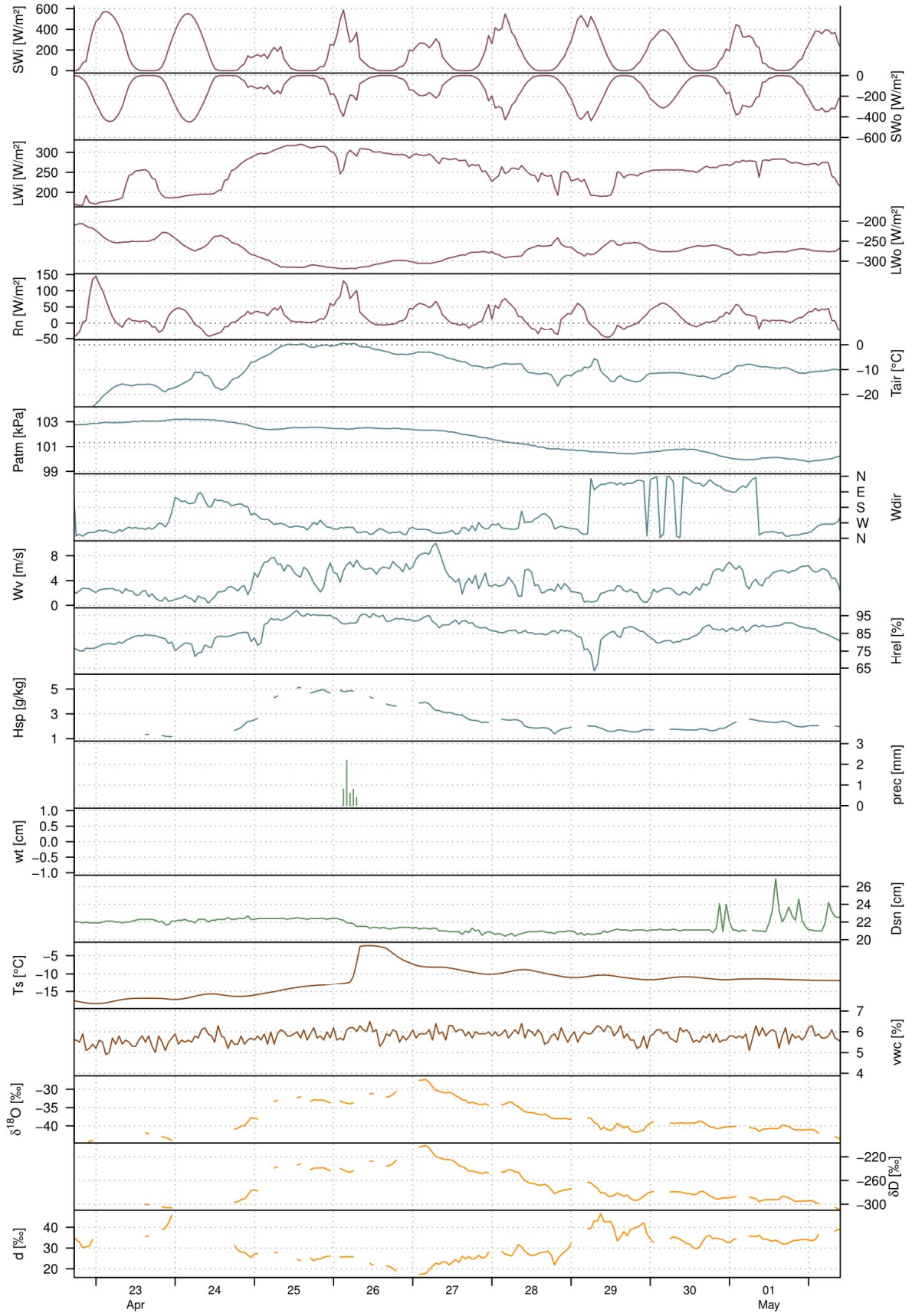

Figure A.7. Time series plot for the isotope peak period 4 (IP4) from 23 April to 01 May 2016 with incoming short-wave radiation (*SWi*), outgoing short-wave radiation (*SWo*), incoming long-wave radiation (*LWi*), outgoing long-wave radiation (*LWo*), net radiation (*Rn*), air temperature at 2 m above ground surface (*Tair*), atmospheric

pressure (*Patm*), wind direction at 3 m above ground surface (*Wdir*), wind speed at 3 m above ground surface (*Wv*), relative humidity at 2 m above ground surface (*Hrel*), specific humidity at 5 m above ground surface (*Hsp*), liquid precipitation (*prec*), water table (*wt*), snow depth (*Dsn*), soil temperature at 1 cm below ground surface (*Ts*), soil liquid volumetric water content at 8 cm below ground surface (*vwc*), δ^{18}O, δD, and deuterium excess (*d*) from top to bottom. The maximum δ values are on 27 April 2016. Colors of the curves signalize the respective environmental group, as defined in this thesis: radiation (*SWi*, *SWo*, *LWi*, *LWo*, *Rn*), air (*Tair*, *Patm*, *Wdir*, *Wv*, *Hrel*, *Hsp*), ground surface (*prec*, *wt*, *Dsn*), soil (*Ts*, *vwc*), and water vapor isotopic composition (δ^{18}O, δD, *d*).

Appendix B Descriptive statistics

Table B.1. Statistical values of all parameters for all data and each period described and analyzed in this thesis. Parameters are incoming short-wave radiation (*SWi*), outgoing short-wave radiation (*SWo*), incoming long-wave radiation (*LWi*), outgoing long-wave radiation (*LWo*), net radiation (*Rn*), air temperature at 2 m above ground surface (*Tair*), atmospheric pressure (*Patm*), wind direction at 3 m above ground surface (*Wdir*), wind speed at 3 m above ground surface (*Wv*), relative humidity at 2 m above ground surface (*Hrel*), specific humidity at 5 m above ground surface (*Hsp*), liquid precipitation (*prec*), water table (*wt*), snow depth (*Dsn*), soil temperature at 1 cm below ground surface (*Ts*), soil liquid volumetric water content at 8 cm below ground surface (*vwc*), $\delta^{18}O$, δD, and deuterium excess (*d*). Periods are the winter onset period (WOP), winter termination period (WTP), and isotope peak periods 1 to 4 (IP1 to IP4). Statistical parameters are mean value (mean), standard deviation (sd), minimum value (min), maximum value (max), and sum per period (sum). All date ranges are inclusive of the last day.

		All data	**WOP**	**WTP**	**IP1**	**IP2**	**IP3**	**IP4**
from		01 Jul 2015	21 Sep 2015	15 May 2016	07 Nov 2015	01 Jan 2016	18 Mar 2016	23 Apr 2016
to		30 Jun 2016	21 Oct 2015	21 Jun 2016	01 Dec 2015	12 Jan 2016	05 Apr 2016	01 May 2016
days		366	31	38	25	12	19	9
SWi	mean	86.6	28.1	238.2	0.4	0.0	112.6	173.7
W/m²	sd	143.3	48.6	194.6	1.9	0.0	135.7	174.5
	min	0.0	0.0	4.1	0.0	0.0	0.0	0.0
	max	710.5	338.4	690.1	28.6	0.3	466.7	588.8
SWo	mean	-42.8	-17.4	-114.9	-0.4	0.0	-89.8	-136.1
W/m²	sd	93.1	29.6	147.8	1.7	0.0	110.1	137.2
	min	-574.8	-182.7	-564.5	-22.5	0.0	-368.3	-450.5
	max	0.0	0.0	0.0	0.0	0.0	0.0	0.0
LWi	mean	241.2	265.5	281.8	209.8	207.2	189.3	257.0
W/m²	sd	68.7	28.7	39.0	36.1	39.9	32.2	39.0
	min	120.1	170.5	188.3	152.3	137.7	147.6	170.2
	max	397.4	316.7	363.9	271.9	289.1	293.2	320.4
LWo	mean	-270.7	-290.0	-322.1	-236.8	-222.4	-228.2	-276.9
W/m²	sd	66.8	17.3	34.5	18.7	26.8	27.8	23.3
	min	-461.4	-323.1	-416.6	-275.8	-290.1	-292.3	-319.0
	max	-158.5	-234.3	-228.7	-192.5	-176.2	-174.0	-223.4
Rn	mean	14.2	-14.5	83.0	-28.0	-15.9	-16.7	17.7
W/m²	sd	78.7	27.2	116.9	22.4	19.6	30.3	32.8
	min	-82.5	-81.5	-57.2	-70.7	-67.4	-73.0	-45.9
	max	487.6	178.6	465.9	5.2	20.5	73.7	144.9
Tair	mean	-11.6	-5.5	0.4	-18.7	-23.0	-20.7	-9.4
°C	sd	15.6	3.8	6.6	4.6	7.4	7.6	5.6
	min	-41.7	-17.0	-19.9	-31.1	-36.2	-36.2	-23.8
	max	24.2	1.4	20.1	-9.3	-5.7	-4.5	0.7
Patm	mean	101.4	101.4	101.2	102.2	101.5	101.5	101.7
kPa	sd	0.9	0.5	0.6	0.7	1.5	0.5	1.1
	min	98.5	99.7	98.6	100.7	98.5	100.4	99.8
	max	104.3	102.5	102.4	103.5	103.5	102.5	103.2

		All data	WOP	WTP	IP1	IP2	IP3	IP4
from		01 Jul 2015	21 Sep 2015	15 May 2016	07 Nov 2015	01 Jan 2016	18 Mar 2016	23 Apr 2016
to		30 Jun 2016	21 Oct 2015	21 Jun 2016	01 Dec 2015	12 Jan 2016	05 Apr 2016	01 May 2016
Wdir	mean	186.8	216.6	185.8	224.7	168.2	203.9	229.2
°	sd	95.8	104.5	108.6	53.2	75.5	82.7	112.7
	min	0.1	0.1	1.3	29.9	1.7	2.2	1.0
	max	360.0	360.0	359.5	335.9	359.0	358.2	355.4
Wv	mean	4.2	4.3	3.9	5.6	4.1	3.6	3.8
m/s	sd	2.4	2.4	1.8	2.7	2.0	3.0	2.1
	min	0.0	0.2	0.1	0.3	0.5	0.1	0.4
	max	14.5	11.5	13.3	13.9	10.7	12.2	10.0
Hrel	mean	80.8	88.7	84.7	79.8	78.1	79.4	86.5
%	sd	9.6	4.9	9.5	5.4	6.9	7.1	5.9
	min	44.9	62.9	44.9	69.9	65.2	66.0	63.5
	max	99.1	97.7	99.1	91.6	94.6	95.6	97.8
Hsp	mean	2.9	3.2	4.3	1.1	0.8	1.2	2.5
g/kg	sd	3.1	0.9	1.6	0.5	0.6	0.7	1.1
	min	0.1	1.2	1.0	0.3	0.2	0.2	1.2
	max	15.8	5.3	9.8	2.4	3.3	3.5	5.1
prec	mean	0.0	0.0	0.0	0.0	0.0	0.0	0.0
mm	sd	0.2	0.0	0.1	0.0	0.0	0.0	0.2
	min	0.0	0.0	0.0	0.0	0.0	0.0	0.0
	max	6.4	1.0	1.8	0.0	0.0	0.0	2.2
	sum	133.8	2.0	12.2	0.0	0.0	0.0	4.8
wt	mean	-0.4	-1.1	-0.4	*N/A*	*N/A*	*N/A*	*N/A*
cm	sd	0.9	0.1	0.8	*N/A*	*N/A*	*N/A*	*N/A*
	min	-3.2	-1.3	-2.2	*N/A*	*N/A*	*N/A*	*N/A*
	max	3.4	-0.9	0.7	*N/A*	*N/A*	*N/A*	*N/A*
Dsn	mean	15.1	8.0	19.6	16.7	15.5	22.8	21.6
cm	sd	10.4	4.6	18.6	2.1	1.0	0.3	0.8
	min	0.0	0.0	0.3	14.2	14.2	21.5	20.4
	max	44.9	15.8	44.9	21.9	21.8	23.4	26.9
Ts	mean	-6.9	-0.2	-2.8	-3.4	-16.8	-19.5	-11.8
°C	sd	11.8	0.3	7.8	1.3	1.7	1.6	3.7
	min	-25.9	-0.8	-12.3	-6.1	-20.2	-23.2	-18.4
	max	19.9	1.5	11.9	-1.4	-13.9	-16.3	-2.2
vwc	mean	33.9	76.2	8.7	7.8	5.7	5.5	5.8
%	sd	39.1	26.7	17.9	0.4	0.3	0.3	0.3
	min	4.6	9.7	5.1	6.6	4.9	4.7	4.9
	max	99.9	98.8	99.4	8.9	6.6	6.4	6.5
δ^{18}**O**	mean	-38.4	-33.4	-35.8	-39.8	-36.3	-42.1	-37.1
‰	sd	6.8	3.3	4.8	3.7	2.8	4.1	4.0
	min	-52.3	-39.4	-45.5	-48.7	-43.8	-50.7	-44.0
	max	-23.2	-25.0	-25.6	-33.1	-32.3	-33.0	-27.4
***δ*D**	mean	-277.8	-235.0	-261.2	-292.5	-272.3	-307.3	-266.6
‰	sd	51.0	23.6	34.4	26.1	19.2	27.9	26.6
	min	-375.2	-285.5	-327.5	-351.7	-324.8	-360.9	-305.9
	max	-164.9	-172.8	-188.7	-243.8	-239.2	-244.0	-201.0

		All data	WOP	WTP	IP1	IP2	IP3	IP4
from		01 Jul 2015	21 Sep 2015	15 May 2016	07 Nov 2015	01 Jan 2016	18 Mar 2016	23 Apr 2016
to		30 Jun 2016	21 Oct 2015	21 Jun 2016	01 Dec 2015	12 Jan 2016	05 Apr 2016	01 May 2016
d	mean	29.3	32.4	25.3	25.9	18.3	29.1	30.4
‰	sd	6.4	4.3	5.6	3.9	3.9	6.9	6.4
	min	6.1	18.7	14.8	19.1	6.1	16.8	17.2
	max	61.3	41.4	41.5	38.1	29.9	49.9	46.6

Selbstständigkeitserklärung

Hiermit versichere ich, dass ich die vorliegende wissenschaftliche Arbeit selbstständig und ohne Hilfe Dritter verfasst habe. Andere als die angegebenen Quellen und Hilfsmittel wurden nicht verwendet. Die den benutzten Quellen wörtlich oder inhaltlich entnommenen Abschnitte sind als solche kenntlich gemacht. Diese wissenschaftliche Arbeit hat in gleicher oder ähnlicher Form noch keiner Prüfungsbehörde vorgelegen und wurde auch nicht veröffentlicht.

Nachname	Schmidt
Vorname	Toni
Matrikelnummer	770881
Studiengang	B.Sc. Geowissenschaften
Titel der Arbeit	Land-atmosphere interactions during winter at a permafrost site in Northern Siberia with a focus on water vapor isotopic composition

Potsdam, den 16. November 2017

Toni Schmidt